

# Diamond formation from hydrocarbon mixtures in planets

Bingqing Cheng,<sup>1,\*</sup> Sebastien Hamel,<sup>2</sup> and Mandy Bethkenhagen<sup>3</sup>

<sup>1</sup>The Institute of Science and Technology Austria, Am Campus 1, 3400 Klosterneuburg, Austria

<sup>2</sup>Lawrence Livermore National Laboratory, Livermore, California 94550, USA

<sup>3</sup>École Normale Supérieure de Lyon, Université Lyon 1,

Laboratoire de Géologie de Lyon, CNRS UMR 5276, 69364 Lyon Cedex 07, France

(Dated: August 4, 2022)

Hydrocarbon mixtures are extremely abundant in the Universe, and diamond formation from them can play a crucial role in shaping the interior structure and evolution of planets. With first-principles accuracy, we first estimate the diamond nucleation rate in pure liquid carbon, and then reveal the nature of chemical bonding in hydrocarbons at extreme conditions. We finally establish the pressure-temperature phase boundary where diamond can form from hydrocarbon mixtures with different atomic fractions of carbon. Notably, we find a depletion zone at pressures above 200 GPa and temperatures below 3000 K-3500 K where diamond formation is thermodynamically favorable regardless of the carbon atomic fraction, due to a phase separation mechanism. The cooler condition of the interior of Neptune compared to Uranus means that the former is much more likely to contain the depletion zone. Our findings can help explain the dichotomy of the two ice giants manifested by the low luminosity of Uranus, and lead to a better understanding of (exo-)planetary formation and evolution.

Carbon and hydrogen are the fourth and the most abundant elements in the Universe [1], and their mixture is the simplest basis to form organic compounds. In our Solar System, the Cassini mission revealed lakes and seas of liquid hydrocarbons on the surface of Titan [2], and the New Horizon spacecraft detected methane frost on the mountains of Pluto [3]. In Neptune and Uranus, methane is a major constituent with a measured carbon concentration from around 2% in the atmosphere [4] and a concentration up to (assumed) 8% in the interior [5]. The methane in the atmosphere absorbs red light and reflects blue light, giving the ice giants their blue hues [6]. Moreover, numerous recently discovered extrasolar planets, some orbiting carbon-rich stars, have spurred a renewed interest in the high-pressure and high-temperature behaviors of hydrocarbons [7].

Diamond nucleation from C/H mixtures is particularly relevant; the "diamonds in the sky" hypothesis [8] suggests that diamonds can form in the mantles of Uranus and Neptune. The diamond formation and the accompanying heat release may explain the long-standing puzzle that Neptune (but not Uranus) radiates much more energy than that it receives from the Sun [9]. Diamond is dense and will gravitate into the core of the ice giants. For white dwarfs, Tremblay *et al.* [10] interpreted the crystallization of the carbon-rich cores to influence the cooling rate.

Many experimental studies have probed the diamond formation from C/H mixtures, but the experiments are extraordinarily challenging to perform and interpret because of the extreme thermodynamic conditions, kinetics, chemical inhomogeneities, possible surface effects from the sample containers, and the need to prove diamond formation inside a diamond anvil cell (DAC). Three DAC studies on methane disagree on the temperature range: Benedetti *et al.* reported diamond formation between 10 to 50 GPa and temperatures of about 2000 K to 3000 K [11]; between 10 to 80 GPa, Hirai *et al.* reported diamond formation above 3000 K [12]; while Lobanov *et al.*

reported the observation of elementary carbon at about 1200 K, and a mixture of solid carbon, hydrogen, and heavier hydrocarbons at above 1500 K [13]. In methane hydrates, Kadobayashi *et al.* reported diamond formation in a DAC between 13 and 45 GPa above 1600 K but not at lower temperatures [14]. Laser shock-compression experiments found diamond formation in epoxy (C,H,Cl,N,O) [15] and polystyrene (-C<sub>8</sub>H<sub>8</sub>-) [16], but none in polyethylene (-C<sub>2</sub>H<sub>4</sub>-) [17].

Moreover, there is a mismatch between the experimental results and theoretical predictions particularly regarding the pressure range of diamond formation. Density functional theory (DFT) combined with crystal structure searches at the static lattice level predicted that diamond and hydrogen are stable at pressures above about 300 GPa [18, 19], while hydrocarbon crystals are stable at lower pressures [18–22]. Based on DFT molecular dynamics (MD) simulations of methane, Ancilotto *et al.* concluded that methane dissociates into a mixture of hydrocarbons below 100 GPa and is more prone to form diamond at above 300 GPa [23], Sherman *et al.* classified the system into stable methane molecules (< 3000 K), a polymeric state consisting of long hydrocarbon chains (4000–5000 K, 40–200 GPa), and a plasma state (> 6000 K) [24]. However, these simulations are constrained to small system sizes and short time scales, so that it is impossible to distinguish between the formation of long hydrocarbon chains and the early stage of diamond nucleation. Using a semi-empirical carbon model, Ghiringhelli *et al.* [25] determined that the diamond nucleation rate in pure liquid carbon is rapid at 85 GPa, 5000 K but negligibly small at 30 GPa, 3750 K, and then extrapolated the nucleation rate to mixtures employing an ideal solution model.

In this work, we go beyond the standard first-principles methods, and study diamond nucleation in C/H mixtures with a fully thermodynamic treatment, by constructing and utilizing machine learning potentials (MLPs) trained on DFT data. To the best of our knowledge, this is the first MLP fitted for high-pressure mixtures. We first quantitatively estimate the nucleation rate of diamond from pure liquid carbon at planetary conditions, considering both the thermodynamic driving

\* bingqing.cheng@ist.ac.at

force and the kinetics. We then reveal the nature of the chemical bonds in C/H mixtures at high-pressure high-temperature conditions. Finally, we determine the thermodynamic driving force of diamond formation in C/H mixtures, taking into account non-ideal effects of mixing. We thereby establish the phase boundary where diamond can possibly form from C/H mixtures at different atomic fractions and  $P$ - $T$  conditions.

### Diamond nucleation in pure liquid carbon

Although planets or stars typically contain a low percentage of carbon [4], it is useful to start with a hypothetical environment of pure carbon. This is to establish the melting line of diamond and an upper bound of the nucleation rate, and to facilitate the subsequent analysis based on C/H mixtures. Moreover, the high-pressure carbon system has experimental relevance in diamond synthesis and Inertial Confinement Fusion applications [32].

Fig. 1a shows the chemical potential difference  $\Delta\mu_D \equiv \mu_{\text{diamond}} - \mu_{\text{liquid C}}$  between the diamond and the pure liquid carbon phases calculated using our MLP at a wide range of pressures and temperatures. Our calculated melting line  $T_m$  of diamond in pure liquid carbon (solid black curve) is compared to other theoretical work and experimental shock-compression data (Fig. 1a). Our  $T_m$  is re-entrant at above 500 GPa, because liquid carbon is denser than diamond at higher pressures. This shape has been observed for the experimental melting line [30]. It was previously predicted using DFT simulations on smaller systems [27–29], but not captured in the free energy calculations performed using a semi-empirical LCBOP carbon model [26].

Although diamond solidification is thermodynamically favorable below the melting line, undercooled liquids can remain metastable for a long time as solidification is initiated by a kinetically activated nucleation process [33]. The classical nucleation theory (CNT) [34] assumes that diamond forms by growing a nanoscopic solid nucleus of size  $n_s$  with free energy

$$G(n_s) = \Delta\mu_D n_s + \gamma(36\pi)^{\frac{1}{3}} v_s^{\frac{2}{3}} n_s^{\frac{2}{3}}. \quad (1)$$

The first (bulk) term stems from the chemical potential difference  $\Delta\mu_D$ . The second (surface) term describes the penalty associated with the interface:  $\gamma$  is the area specific interfacial free energy,  $v_s$  is the molar volume of diamond, and  $(36\pi)^{\frac{1}{3}}$  is a geometrical constant.

Nucleation is thus typically a rare event that does not occur during a conventional MD simulation at a reasonable undercooling. To accelerate the sampling so as to obtain a reversible formation of a solid nucleus in simulations, we performed metadynamics at pressures between 25 GPa and 600 GPa, and an undercooling ranging between 8% and 20%. A diamond nucleus formed during a metadynamics run is illustrated in Fig. 1b. Most of the nucleus consists of cubic diamond. Occasionally hexagonal diamond structures form, usually near the solid-liquid interface.

Fig. 1c shows examples of  $G(n_s)$  extracted from the metadynamics simulations, applying the framework introduced in

Ref. [35]. These free energy profiles at different conditions, combined with the previously computed  $\Delta\mu_D$ , are then fitted to the CNT expression (Eqn. (1)), to obtain the surface energy  $\gamma(36\pi)^{\frac{1}{3}} v_s^{\frac{2}{3}}$  as the only fitting parameter. The surface energy is then extrapolated to other conditions using a linear fit in both  $P$  and  $T$ .

The nucleation rate is obtained from the CNT free energy profile [36]:

$$J = (1/v_l) Z f^+ \exp(-G^*/k_B T), \quad (2)$$

where the nucleation barrier  $G^* = \max(G(n_s)) = G(n_s^*)$  is the free energy of the critical nucleus with size  $n_s^*$ ,  $v_l$  is the molar volume of the undercooled liquid,  $f^+$  is the addition rate of particles to the critical nucleus, and the Zeldovich factor

is  $Z = \sqrt{\frac{d^2 G(n_s)}{2\pi k_B T dn_s^2}} \Big|_{n_s=n_s^*}$ . As detailed in the Supplementary Information, we computed  $f^+$  accurately and directly at  $T=5000$  K and  $P=50$  GPa from umbrella sampling trajectories, by applying a stochastic model [37]. To estimate  $f^+$  at other conditions, we express the addition rate as [33]:  $f^+ \propto D n_s^{2/3}$ , where  $D$  is the self-diffusion coefficient of the carbon atoms in the liquid.

Combining all these pieces, we obtain the nucleation rate  $J$  for diamond in pure liquid carbon in Fig. 1d. Within a few hundred Kelvin below  $T_m$ , or about 5% of undercooling, there is a region with negligible nucleation rate;  $J = 10^{-40} \text{ m}^{-3} \text{ s}^{-1}$  means that not a single critical nucleus of diamond will form in a planet-sized body during the lifetime of the Universe. The  $J$  increases rapidly as the temperature decreases, making homogeneous diamond nucleation almost instantaneous at more than about 500 K of undercooling. The only previous study that has determined the diamond nucleation rate is by Ghiringhelli *et al.* [25] using the LCBOP carbon model: at point A=(30 GPa, 3750 K),  $J_A = 10^{30} \text{ m}^{-3} \text{ s}^{-1}$ ; and at point B=(85 GPa, 5000 K),  $J_B = 10^{-80} \text{ m}^{-3} \text{ s}^{-1}$ . In our calculations,  $J_A = 10^{23} \text{ m}^{-3} \text{ s}^{-1}$  and  $J_B = 10^{25} \text{ m}^{-3} \text{ s}^{-1}$ . As such, we roughly agree with Ghiringhelli *et al.* for point A, but disagree for point B. The discrepancy originates from the estimation of the surface energy: our  $\gamma$  is only weakly dependent on pressure with  $\gamma_A = 2.0 \text{ J/m}^2$  and  $\gamma_B = 2.1 \text{ J/m}^2$ , while Ghiringhelli *et al.* predicted a much stronger pressure dependence with  $\gamma_A = 1.86 \text{ J/m}^2$  and  $\gamma_B = 3.5 \text{ J/m}^2$ . The discrepancy may be due to the different underlying interatomic potentials. Overall, we find that the pure carbon system is deeply undercooled at the  $P$ - $T$  conditions in the two icy planets (green and orange lines in Fig. 1d) and will nucleate instantly.

### The nature of C-H bonds

Going beyond the pure carbon case, we investigate the nature of the chemical bonds in C/H mixtures at conditions relevant for planetary interiors. The high-pressure behavior of hydrocarbons is also crucial in many shock-compression experiments for the development of fusion energy platforms and Inertial Confinement Fusion capsules [38]. The properties of the covalent C-C and C-H bonds are well-known at ambient

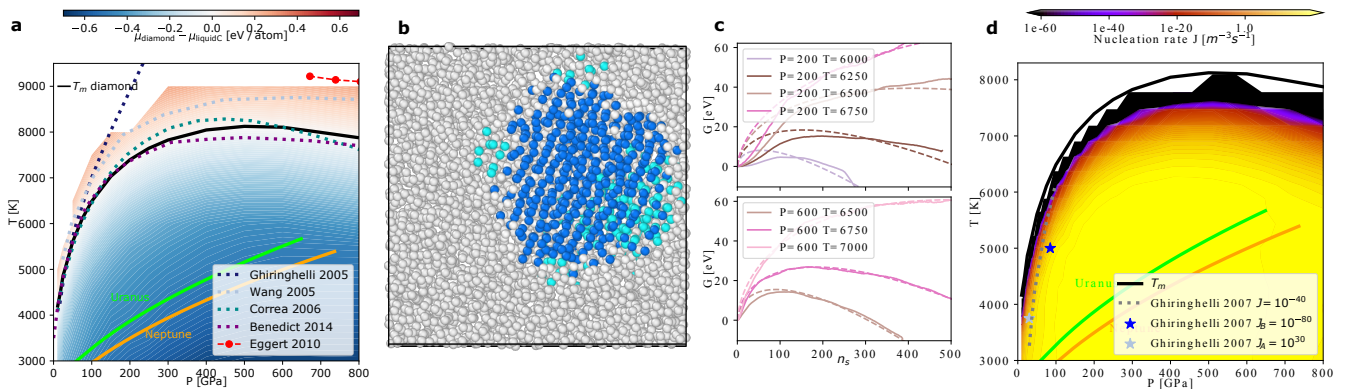


FIG. 1. Thermodynamics and kinetics for diamond formation in pure liquid carbon.

**a** The chemical potential of diamond,  $\Delta\mu_D$ , referenced to pure liquid carbon. The stability region of graphite at  $P \lesssim 10$  GPa is not shown. The melting curve  $T_m$  is compared to previous calculations using thermodynamic integration (TI) employing a semi-empirical potential by Ghiringhelli *et al.* [26], TI using DFT by Wang *et al.* [27], coexistence DFT simulations by Correa *et al.* [28], an analytic free-energy model fitted to DFT data by Benedict *et al.* [29], and a shock-compression experiment by Eggert *et al.* [30].

**b** A snapshot of atomic positions from metadynamics simulations at 300 GPa, 6500 K. Blue atoms are identified as having cubic diamond local structures, and the turquoise ones have hexagonal diamond structures.

**c** Nucleation free energy profiles as functions of nucleus sizes  $n_s$  at selected conditions. The dashed curves are the fits to the CNT expression in Eqn. (1).

**d** The estimated homogeneous nucleation rate of diamond from pure liquid carbon. Stars indicate the direct estimates of  $J$  by Ghiringhelli *et al.* [25], and the dotted line shows their inferred threshold conditions with a nucleation rate of  $10^{-40} \text{m}^{-3} \text{s}^{-1}$ .

The  $P$ - $T$  curves of planetary interior conditions for Uranus (green line) and Neptune (orange line) shown in **a** and **d** are from Ref. [31].

conditions, but it is unclear how extreme conditions affect these bonds. DFT studies coupled with harmonic approximations have predicted a variety of hydrocarbon crystals to be stable at  $P \leq 300$  GPa [18–22], but these studies are restricted to low temperatures as the melting lines of hydrogen and methane are below 1000 K and 2000 K, respectively, while harmonic approximations break down completely for these liquids.

We performed MD simulations using our fully dissociable MLP for C/H mixtures over a wide range of thermodynamic conditions. We focus on the  $\text{CH}_4$  composition to directly compare to previous studies. Other compositions can be analyzed in the same way and yield qualitatively similar behaviors. At  $T < 2500$  K, the MD is not ergodic within the simulation time of 100 ps, and therefore analysis is performed only at temperatures above this threshold. Fig. 2a shows the snapshots of carbon bonds from the MD simulations of the  $\text{CH}_4$  system. At 4000 K and  $P = 100$  GPa, 200 GPa, and 600 GPa, the system is primarily composed of various types of hydrocarbon chains. The formation of longer chains at higher pressures is consistent with the observations in previous DFT MD studies [23, 24], although the DFT simulations have severe finite size effects because polymer chains consisting of just a few carbon atoms can connect with their periodic images and become infinitely long. At high pressures, the chains assemble carbon networks, and the system shows more obvious signs of spatial inhomogeneity of carbon atoms.

In our chemical bond analysis, a C-C bond is identified whenever the distance between a pair of carbon atoms is within 1.6 Å, and a C-H bond is defined using a cutoff of 1.14 Å. These cutoffs correspond to the first neighbor shells of the C-C and C-H radial distribution functions, respectively. The

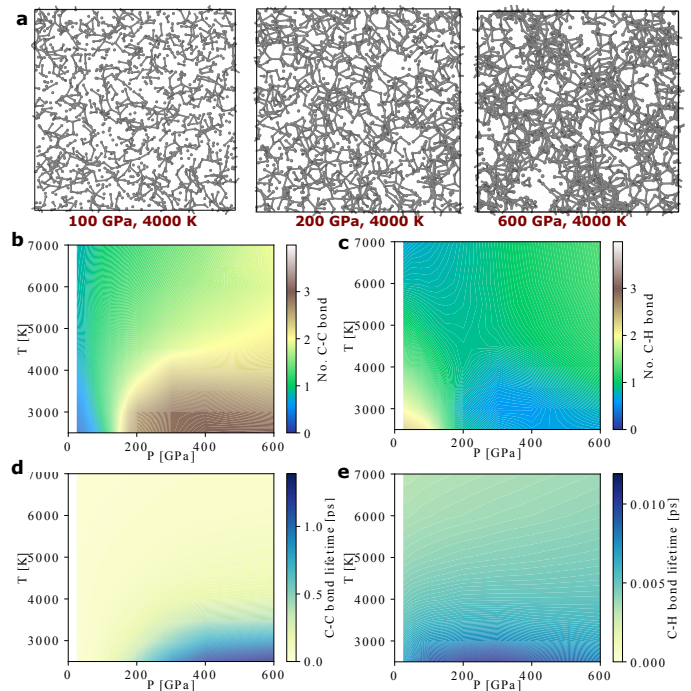


FIG. 2. Bonding behavior in the  $\text{CH}_4$  mixture at high-pressure high-temperature conditions.

**a** Snapshots from MD simulations using the MLP. Carbon atoms are shown as small gray spheres, while hydrogen atoms are not drawn for clarity. Bonds are drawn for C-C pairs with distances within 1.6 Å.

**b,c** Average number of C-C bonds (**b**) and C-H bonds (**c**) per carbon atom from MD simulations of  $\text{CH}_4$  composition.

**d,e** Average lifetimes of the C-C bonds (**d**) and C-H bonds (**e**).

average number of C-C and C-H bonds at different conditions are shown in Fig. 2b,c. The number of bonds varies smoothly as a function of  $P$  and  $T$ . The average number of the C-C bonds decreases with temperature, suggesting that at  $T \geq 2500$  K the system is not made of hydrocarbon crystals that were predicted to be stable at low temperatures in previous DFT studies [18–22]. The average number of C-H bonds for each carbon atom is close to one at all conditions considered here even though the overall composition is  $\text{CH}_4$ , indicating that most hydrogen atoms are not bonded to any carbons.

To determine the lifetimes of the C-C and the C-H bonds, we recorded the time it takes for a newly formed bond to dissociate during the MD simulations. Fig. 2d-e show the average bond lifetimes. The C-H bond lifetimes are extremely short, less than about 0.01 ps. The C-C bonds are more long-lived, yet only have a mean lifetime of less than about 1 ps at all the conditions considered here. Such short lifetimes are consistent with previous DFT MD simulations of  $\text{CH}_4$  [24]. The short bond lifetimes indicate that the hydrocarbon chains in the systems decompose and form quickly. In other words, the C/H mixture behaves like a liquid with transient C-C and C-H bonds.

### Thermodynamics of C/H mixtures

We then determine the chemical potentials of carbon in C/H mixtures,  $\Delta\mu^C(\chi_C)$ , as a function of the atomic fraction of carbon,  $\chi_C = N_C/(N_C + N_H)$ . This, combined with the chemical potential difference  $\Delta\mu_D$  between diamond and pure carbon liquid, establishes the thermodynamic phase boundary for diamond formation from C/H mixtures with varying atomic ratios.

Dilution will usually lower the chemical potential of carbon in a mixture, which can be understood from the ideal solution assumption:  $\mu_{id}^C = k_B T \ln(\chi_C)$ . However, the ideal solution model neglects the atomic interactions and cannot capture possible liquid-liquid phase separations. To consider non-ideal mixing effects, we compute the chemical potentials of mixtures using the MLP. This is not an easy task, because traditional particle insertion methods [39] fail for this dense liquid system, and thermodynamic integration from an ideal gas state to the real mixture [40] is not compatible with the MLP. We employ the newly developed S0 method [41]:

$$\left(\frac{d\mu^C}{d\ln\chi_C}\right)_{T,P} = \frac{k_B T}{(1-\chi_C)S_{CC}^0 + \chi_C S_{HH}^0 - 2\sqrt{\chi_C(1-\chi_C)}S_{CH}^0}, \quad (3)$$

where  $S_{CC}^0$ ,  $S_{CH}^0$ , and  $S_{HH}^0$  are the values of the static structure factor between the said types of atoms at the limit of infinite wavelength [41], which can be determined from equilibrium MD simulations of a C/H mixture with a given carbon fraction  $\chi_C$ .  $\mu^H$  is then fixed using the Gibbs-Duhem equation. Note that only the relative chemical potential is physically meaningful, and we conveniently select the reference states to be the pure carbon and hydrogen liquids, i.e.  $\mu^C(\chi_C = 1) = 0$  and  $\mu^H(\chi_C = 0) = 0$ . We obtained  $\mu^C$  and  $\mu^H$  at different  $\chi_C$  on a grid of  $P$ - $T$  conditions between 10 GPa–600 GPa and

3000 K–8000 K, by numerically integrating  $d\mu^C/d\ln\chi_C$ .

$d\mu^C/d\ln\chi_C$  at  $P = 50$  GPa,  $T = 4000$  K and  $P = 400$  GPa,  $T = 3000$  K are shown in Fig. 3a,d, respectively. For both sets, these values deviate from the ideal behavior (i.e. constant at 1), and have maxima and minima around certain compositions. The corresponding chemical potentials are plotted in Fig. 3b,e, while the results at other conditions are shown in Fig. M4 of the Methods. As an independent validation, we also computed  $\mu^C$  using the coexistence method described in the Methods, although this approach is in general less efficient and can become prohibitive if carbon concentration or diffusivity is low. The values from the coexistence method are shown as the hollow symbols in Fig. 3b, in agreement with the S0 method.

In both Fig. 3b and e,  $\mu^C$  has a plateau at  $\chi_C$  between about 0.25 and 0.35, and the same phenomenon is found at  $T \leq 5000$  K at 50 GPa, and at even broader temperature range under increasing pressures, up to 8000 K at 600 GPa (see Fig. M4 of the Methods). At 50 GPa, 4000 K (Fig. 3b),  $\mu^C$  then decreases rapidly and approaches the ideal behavior at lower  $\chi_C$ . In contrast, at 400 GPa, 3000 K (Fig. 3e),  $\mu^C$  plateaus and reaches a constant value for  $\chi_C < 0.12$ . The plateaus at low  $\chi_C$  were observed at pressures between 200 GPa and 600 GPa and temperatures lower than 3500 K (see Fig. M4 of the Methods). In Fig. 3b,e, the chemical potentials of diamond,  $\mu_D$ , are indicated by black diamond symbols and horizontal lines. If  $\mu^C$  is larger than  $\mu_D$  at a given  $\chi_C$ , diamond formation is thermodynamically favorable.

To rationalize the plateaus, we express the per-atom chemical potential of the C/H mixture as

$$\mu_{mixture}(\chi_C) = \chi_C \mu^C(\chi_C) + (1 - \chi_C) \mu^H(\chi_C), \quad (4)$$

and compare it to the ideal solution curve  $\mu_{mixture,id} = k_B T (\chi_C \log(\chi_C) + (1 - \chi_C) \log(1 - \chi_C))$ . Fig. 3c shows  $\mu_{mixture}$  at 50 GPa, 4000 K. Compared with the ideal solution chemical potential (dashed gray curve) which is fully convex,  $\mu_{mixture}$  has two edges. One can thus perform a common tangent construction to the  $\mu_{mixture}$  curve to find out the co-existing liquid phases. The green line in Fig. 3d indicates the common tangent, and the two green crosses shows the location of the edges. For C/H mixtures with  $\chi_C$  between the two atomic ratios ( $\chi_C^1 = 0.27$  and  $\chi_C^2 = 0.36$  at the condition shown), a liquid-liquid phase separation (PS1) will occur and form two phases with the proportions determined by the lever rule. Here the region between the two edges is not concave but linear, which is because the phase separation has little activation barrier and already occurs during the MD simulations. In other words, a C/H mixture with a carbon fraction that is between the values of  $\chi_C^1$  and  $\chi_C^2$  will first undergo spontaneous liquid-liquid phase separation, which explains the corresponding plateaus in  $\mu^C$  of Fig. 3b,e.

Furthermore, Fig. 3f shows that, at 400 GPa, 3000 K,  $\mu_{mixture}$  at low  $\chi_C$  significantly deviates from the ideal solution approximation (dashed gray curve), and one can construct a tangent as plotted in purple. This means that, besides the aforementioned PS1, C/H mixtures at a low C fraction can also phase separate (PS2) into a fluid of mostly hydrogen and another fluid with  $\chi_C \approx 0.12$  (purple cross). We show example snapshots of such phase separated configurations collected

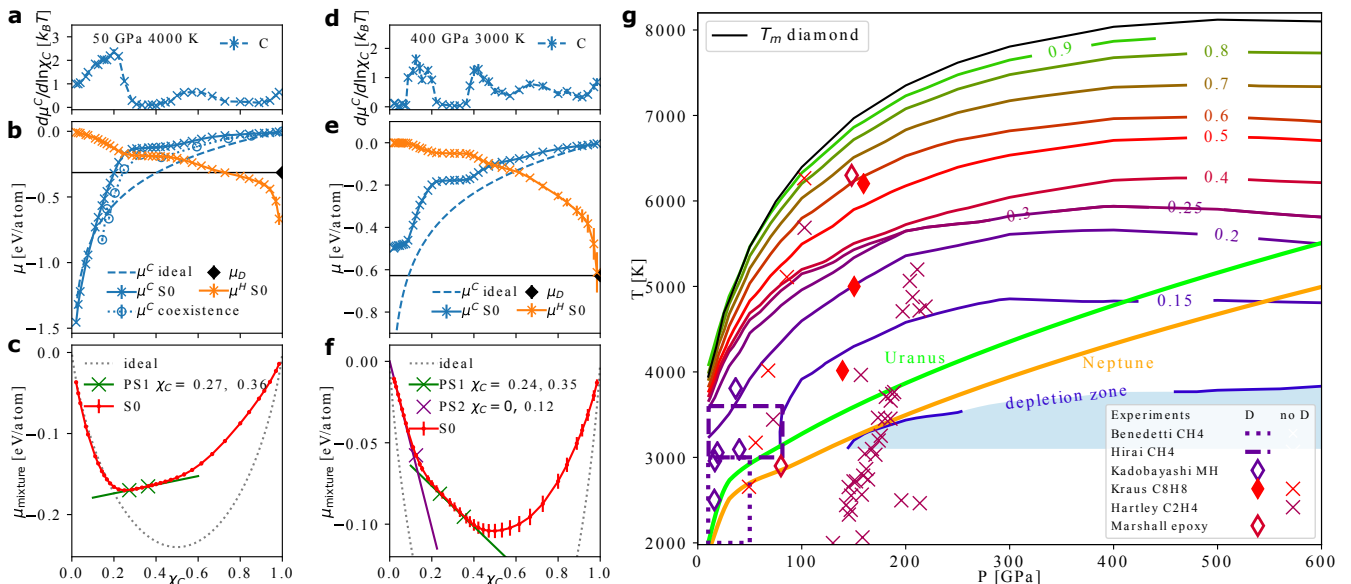


FIG. 3. Thermodynamic behaviors of C/H mixtures.

**a,d**  $d\mu^C/d\ln(\chi_C)$  computed from static structure factors using Eqn. (3), at 50 GPa, 4000 K (**a**) and at 400 GPa, 3000 K (**d**).

**b,e** The chemical potential per carbon atom in C/H mixtures, estimated using the S0 method (blue crosses connected by solid curve), the coexistence method (blue hollow symbols connected by dotted curve), and the ideal solution approximation (blue dashed curve). The chemical potential per hydrogen atom is shown as orange line with crosses. The chemical potential of diamond is indicated by the black diamond symbol and the black horizontal line.

**c,f** The free energy per atom of C/H mixtures with different carbon fractions. The free energy of the ideal solution is shown as dashed gray curve, and the result from the S0 method is shown in red. The green line illustrates the constructed double tangent, and the two green crosses show the composition of the liquids forming after phase separation (PS1). The purple line is a tangent and the purple cross shows the composition of the more carbon-rich phase after PS2.

**g** The conditions below which diamond formation is thermodynamically possible at different carbon ratios (colored solid lines). The shaded area below the bright blue line indicates the depletion zone, where diamond formation is thermodynamically favorable regardless of the carbon ratio. Experimental observation of diamonds (D) is indicated by diamond symbols and dashed/dotted rectangular regions, while no diamond observation (no D) is marked by cross symbols: laser-heated DAC data for methane [11, 12], for methane hydrate (MH) [14], and shock-compression experiments for polystyrene ( $-\text{C}_8\text{H}_8-$ ) [16], polyethylene ( $-\text{C}_2\text{H}_4-$ ) [17], and epoxy [15]. The symbols are colored according to the  $N_C/(N_C + N_H)$  ratio of the starting materials, using the same color scheme for the phase boundaries. The  $P$ - $T$  curves of planetary interior conditions for Uranus (green line) and Neptune (orange line) are from Ref. [31].

from the MD simulations in the Supplementary Information. This PS2 explains the plateau of  $\mu^C$  at low  $\chi_C$  in Fig. 3d, as the carbon concentrations in both phase-separated liquids stay the same, while only the proportions of the two liquids change. This phase separation has immense consequences: at pressures above 200 GPa and temperatures below 3000 K–3500 K, C in C/H mixtures will always have  $\mu^C > \mu_D$  even at very low C fraction due to PS2, and the carbon atoms will thus always be under a thermodynamic driving force to form diamond. We refer to these conditions as the “depletion zone”.

Fig. 3g presents the thermodynamic phase boundaries, below which diamond formation is possible in C/H mixtures for each indicated carbon atomic fraction. This is obtained by combining the values of  $\mu^C(\chi_C)$  in C/H mixtures and  $\mu_D$  at a wide range of  $P$ - $T$  conditions. For lower and lower  $\chi_C$ , the boundaries deviate more and more from the  $T_m$  of diamond. At  $P < 100$  GPa, the locations of the boundaries are very sensitive to both temperature and pressure, whereas at higher  $P$  it is mostly independent of pressure. Fig. 3g can also be read in another way: for a certain  $P$ - $T$  condition, it gives the minimal

carbon ratio required to make diamond formation possible. Notice that the  $\chi_C = 0.25$  and  $\chi_C = 0.3$  lines almost overlap, which is due to the plateau of  $\mu^C$  induced by PS1. The light blue shaded area indicates the depletion zone, where diamond formation is always possible due to PS2. In this zone, carbon atoms will first form a carbon-rich liquid phase, and diamond can nucleate from this phase. Such process is similar with a two-step nucleation mechanism previously revealed in protein systems [42].

Previous experimental measurements are included in Fig. 3g, with the conditions where diamonds were either found (diamond symbols or rectangular regions) or absent (cross symbols) indicated. At lower pressures, our calculations largely agree with the observation of diamond formation for methane in DAC experiments between 2000–3000 K [11] and above 3000 K [12]. We find less agreement with the shock-compression experiments at higher pressures [16, 17], which may be due to the kinetic effects in the rapid compression and/or the difficulty in the temperature estimation of these experiments. The hollow diamond symbols in Fig. 3g

show the diamond formation conditions from starting materials of more complex compositions: Marshall *et al.* [15] used epoxy (C:H:Cl:N:O  $\approx$  27:38:1:1:5) and Kadobayashi *et al.* [14] used methane hydrate. We find little agreement between Kadobayashi *et al.* [14] and our phase boundaries, if we compare solely in terms of  $\chi_C$  including all atomic species, although the agreement is improved if based on the  $\chi_C$  of methane alone, and indeed CH<sub>4</sub> may be an intermediate product in the experiment [14]. The liquid-liquid phase separations of C/H mixtures have not been previously observed, but they may be detected from speed of sound, mixed optical spectra, inhomogeneity in the diamond formation reaction, and hydrodynamic instability during compression experiments.

## DISCUSSIONS

We first quantified the thermodynamics and kinetics of the diamond nucleation in pure liquid carbon, which sets an upper bound for the conditions of diamond formation in C/H mixtures. We then showed that C/H mixtures behave like liquids at  $T \geq 2500$  K, and precisely computed the thermodynamic boundary of diamond formation for different atomic ratios. Notably, we revealed the occurrence of phase separations of C/H mixtures and its role in diamond formation. At  $200 < P < 600$  GPa and  $T$  below 3000 K-3500 K, there is a depletion zone where phase separation can happen and diamond may form in the carbon-rich phase.

Our phase boundaries in Fig. 3g put largely scattered experimental measurements [11, 12, 15–17] into context, and provide a mechanistic understanding of the thermodynamics involved. They also help gauge the accuracy of the experimental determination of diamond formation conditions, extrapolate between different experiments, and guide future efforts to validate these boundaries. Note that our boundaries are solely based on the thermodynamic criterion, but the kinetic nucleation rate may play a role particularly in shock-compression experiments. In simulations of pure carbon liquid, we found the homogeneous nucleation rate to be rapid when the undercooling is more than about 5%. A different amount of undercooling may be needed for diamond nucleation from C/H mixtures, depending on the magnitude of the interfacial free energy contribution (Eqn. (1)). In experiments, DAC are in close contact with the fluid samples, so heterogeneous nucleation may happen, which requires less undercooling compared with the homogeneous case. In addition, other elements (e.g. He, N, O) are also prevalent in icy planets, and we suggest future experiments to probe how they affect the phase boundaries of diamond formation.

The “depletion zone” can help explain the difference in the luminosity between Uranus and Neptune. Being similar in size and composition, Neptune has a strong internal heat source but Uranus does not [43]. The “diamonds in the sky” hypothesis [8, 11] relates the heat source with diamond formation, but does not explain the dichotomy between the two planets. By comparing the  $P$ - $T$  conditions at different depths of the two ice giants from Ref. [31] with our calculated phase boundaries (in Fig. 3g), one can see that a relatively small difference in

the planetary profile can drastically change the possibility of diamond formation: At the  $P$ - $T$  conditions in Uranus, diamond formation requires about 15% of carbon, which seems unlikely as less than 10% of carbon is believed to be present in its mantle [4]. As such, diamond formation in Uranus may be absent. In contrast, Neptune is a bit cooler so it is much more likely that its planetary profile may have an overlap with the depletion zone; at these conditions C/H mixtures will phase separate (PS2), and diamond formation is thermodynamically favorable regardless of the actual carbon fraction. If there is indeed an overlap, diamonds can form in the depletion zone in the mantle of Neptune, and then sink towards the core while releasing heat. Although the mantle will become increasingly carbon-depleted, the diamond formation in the depletion zone can proceed until all carbon is exhausted. Moreover, the “diamond rain” will naturally induce a compositional gradient inside the planet, which is an important aspect in explaining the evolution of giant planets [44, 45].

Our carbon-ratio-dependent diamond formation phase boundaries can help estimate the prevalence and the existence criteria of extraterrestrial diamonds. Neptune-like exoplanets are extremely common according to the database of planets discovered [46], and methane-rich exoplanets are modeled to have a carbon core, a methane envelope, and a hydrogen atmosphere [7]. Our boundaries can put a tight constraint on the structure and composition of these planets. Furthermore, diamond formation and liquid-liquid phase separation play a key role in the cooling process in white dwarfs [10], and thus the precise determination for the onset of phase separation and crystallization is also crucial there.

**Acknowledgments** BC thanks Daan Frenkel for stimulating discussions. We thank Aleks Reinhardt, Daan Frenkel, Marius Millot, Federica Coppari, Rhys Bunting, and Chris J. Pickard for critically reading the manuscript and providing useful suggestions. BC acknowledges resources provided by the Cambridge Tier-2 system operated by the University of Cambridge Research Computing Service funded by EPSRC Tier-2 capital grant EP/P020259/1. SH acknowledges support from LDRD 19-ERD-031 and computing support from the Lawrence Livermore National Laboratory (LLNL) Institutional Computing Grand Challenge program. Lawrence Livermore National Laboratory is operated by Lawrence Livermore National Security, LLC, for the U.S. Department of Energy, National Nuclear Security Administration under Contract DE-AC52-07NA27344. MB acknowledges support by the European Horizon 2020 program within the Marie Skłodowska-Curie actions (xICE grant number 894725) and computational resources at the North-German Supercomputing Alliance (HLRN) facilities.

**Authors contributions:** B.C., S.H., and M.B. conceived the idea of studying high-pressure methane; B.C. designed the research; B.C. performed the simulations related to the MLP; B.C., S.H., and M.B. performed the DFT calculations; B.C., S.H., and M.B. wrote the paper.

**Competing interests:** All authors declare no competing interests.

**Data availability statement** All original data generated for the study, including the MLP, the training set, simulation input

files, intermediate data, PYTHON notebook, are in the SI repository (url to be inserted)

## METHODS

*DFT calculations* Single-point DFT calculations with VASP [47–50] were carried out for configurations with various C/H ratios to generate the training set of the MLP. The simulations were performed with the Perdew–Burke–Ernzerhof (PBE) exchange–correlation functional [51] employing hard pseudopotentials for hydrogen and carbon, a cutoff energy of 1000 eV, and a consistent k-point spacing of  $0.2 \text{ \AA}^{-1}$ . In addition, extensive PBE MD simulations for  $\text{CH}_{16}$ ,  $\text{CH}_8$ ,  $\text{CH}_4$ ,  $\text{CH}_2$ ,  $\text{CH}$ ,  $\text{C}_2\text{H}$  and  $\text{C}_4\text{H}$  mixtures were performed, and together with previous PBE MD data for methane [52], carbon [29] and hydrogen [53], were used to benchmark the MLP.

*Machine learning potential* We generated flexible and dissociable MLPs for the high-pressure C/H system, employing the Behler–Parrinello artificial neural network [54], and using the N2P2 code [55]. The total training set contains 92,185 configurations with a sum of 8,906,582 atoms, and was constructed using a combination of strategies including DFT MD, random structure searches, adapting previous training sets for pure C [56] and H [53], and active learning. Details on the construction and the benchmarks of the MLP are provided in the Supplementary Information.

*MLP MD simulation details* All MD simulations were performed in LAMMPS [57] with a MLP implementation [58]. The time step was 0.25 fs for C/H mixtures, and 0.4 fs for pure carbon systems.

*Computing the chemical potentials of diamond and pure liquid carbon* We computed  $\Delta\mu_D$  using interface pinning simulations [59], which were performed using the PLUMED code [60]. We used solid-liquid systems containing 1,024 C atoms at pressures between 10–800 GPa and at temperatures close to the melting line, employing the MLP. The Nosé–Hoover barostat was used only along the  $z$  direction that is perpendicular to the interface in these coexistence simulations, while the dimensions of the supercell along the  $x$  and  $y$  directions were commensurate with the equilibrium lattice parameters of the diamond phase at the given conditions. We used the locally-averaged [61]  $Q_3$  order parameter [62] for detecting diamond structures, and introduced an umbrella potential to counter-balance the chemical potential difference and constrain the size of diamond in the system. We then used thermodynamic integration along isotherms and isobars [63, 64] to extend the  $\Delta\mu_D$  to a wide range of pressures and temperatures.

*Metadynamics simulations for nucleation* Well-tempered metadynamics [65] simulations with adaptive bias [66] were performed using the PLUMED code [60] on pure carbon systems with 4,096 atoms in a cubic box. The collective variable (CV) is the number of atoms that have the diamond structure, identified using the locally-averaged [61]  $Q_3$  order parameter [62]. The specification of this CV in PLUMED is provided in the Supplementary Information, along with all the nucle-

ation free energy profiles computed.

*MLP MD simulation of  $\text{CH}_4$*  The simulation cell contained 7,290 atoms (1,458  $\text{CH}_4$  formula units). Each simulation was run for more than 100 ps. The simulations were performed in the NPT ensemble, using the Nosé–Hoover thermostat and isotropic barostat. At each condition, two independent MD simulations were initialized using a starting configuration of either bonded  $\text{CH}_4$  molecules on a lattice or a liquid. For  $T \geq 2500 \text{ K}$ , the two simulations provided consistent statistical properties. These simulations were the basis for the further analysis we performed. For  $T < 2500 \text{ K}$  the two runs gave different averages, meaning that under these conditions the system is not ergodic within the simulation time.

*Computing the chemical potentials of C in C/H mixtures* We used two independent methods for computing the chemical potentials of carbon in C/H mixtures at various conditions. The first is the S0 method [41] that uses the static structure factors computed from equilibrium NPT simulations. The simulations were performed on a grid of  $P$ - $T$  conditions,  $P=10 \text{ GPa}$ ,  $25 \text{ GPa}$ ,  $50 \text{ GPa}$ ,  $100 \text{ GPa}$ ,  $200 \text{ GPa}$ ,  $300 \text{ GPa}$ ,  $400 \text{ GPa}$ ,  $600 \text{ GPa}$ , and  $T=3500 \text{ K}$ ,  $4000 \text{ K}$ ,  $5000 \text{ K}$ ,  $6000 \text{ K}$ ,  $7000 \text{ K}$ , and  $8000 \text{ K}$ . At each  $P$ - $T$  condition, MD simulations were run for systems at varying atomic ratios, on a dense grid of  $\chi_C$  from 0.015 to 0.98. The system size varied between 9,728 and 82,944 total number of atoms. We obtained the static structure factors at different wavevectors  $\mathbf{k}$  using the Fourier expansion on the scaled atomic coordinates, i.e.

$$S_{AB}(\mathbf{k}) = \frac{1}{\sqrt{N_A N_B}} \left\langle \sum_{i=1}^{N_A} \exp(i\mathbf{k} \cdot \hat{\mathbf{r}}_{i_A}(t)) \sum_{i=1}^{N_B} \exp(-i\mathbf{k} \cdot \hat{\mathbf{r}}_{i_B}(t)) \right\rangle \quad (5)$$

where  $AB$  can be CC, CH and HH, and  $\hat{\mathbf{r}}(t) = \mathbf{r}(t) \langle l \rangle_{\text{NPT}} / l(t)$  and  $l(t)$  is the instantaneous dimension of the supercell. We then determined  $S_{CC}^0$ ,  $S_{CH}^0$  and  $S_{HH}^0$  by extrapolating  $S_{AB}(\mathbf{k})$  to the  $\mathbf{k} \rightarrow 0$  case using the Ornstein–Zernike form as described in Ref. [41]. Finally, we used numerical integration using Eqn.3 of the main text to obtain the chemical potential of carbon for different atomic fractions, and get the chemical potential of H using the Gibbs–Duhem equation. All the chemical potential data are presented in Fig. M4.

The second approach is based on the coexistence method, similar to the setup used for computing the chemical potentials of the pure carbon systems. In this case, interface pinning simulations [37, 59] were performed on a diamond–C/H liquid coexistence system containing 1024 C atoms and a varying number of H atoms at pressures 0–600 GPa. A snapshot of the coexistence system is provided in the Supplementary Information. The chemical potentials estimated using coexistence are shown in Fig. M4, and the errors shown are the standard errors of the mean estimated from the values of the CV. However, there are other sources of errors that are hard to estimate: finite size effects and ergodicity issues related to the explicit interface; the carbon concentration can vary in the liquid region of the simulation box.

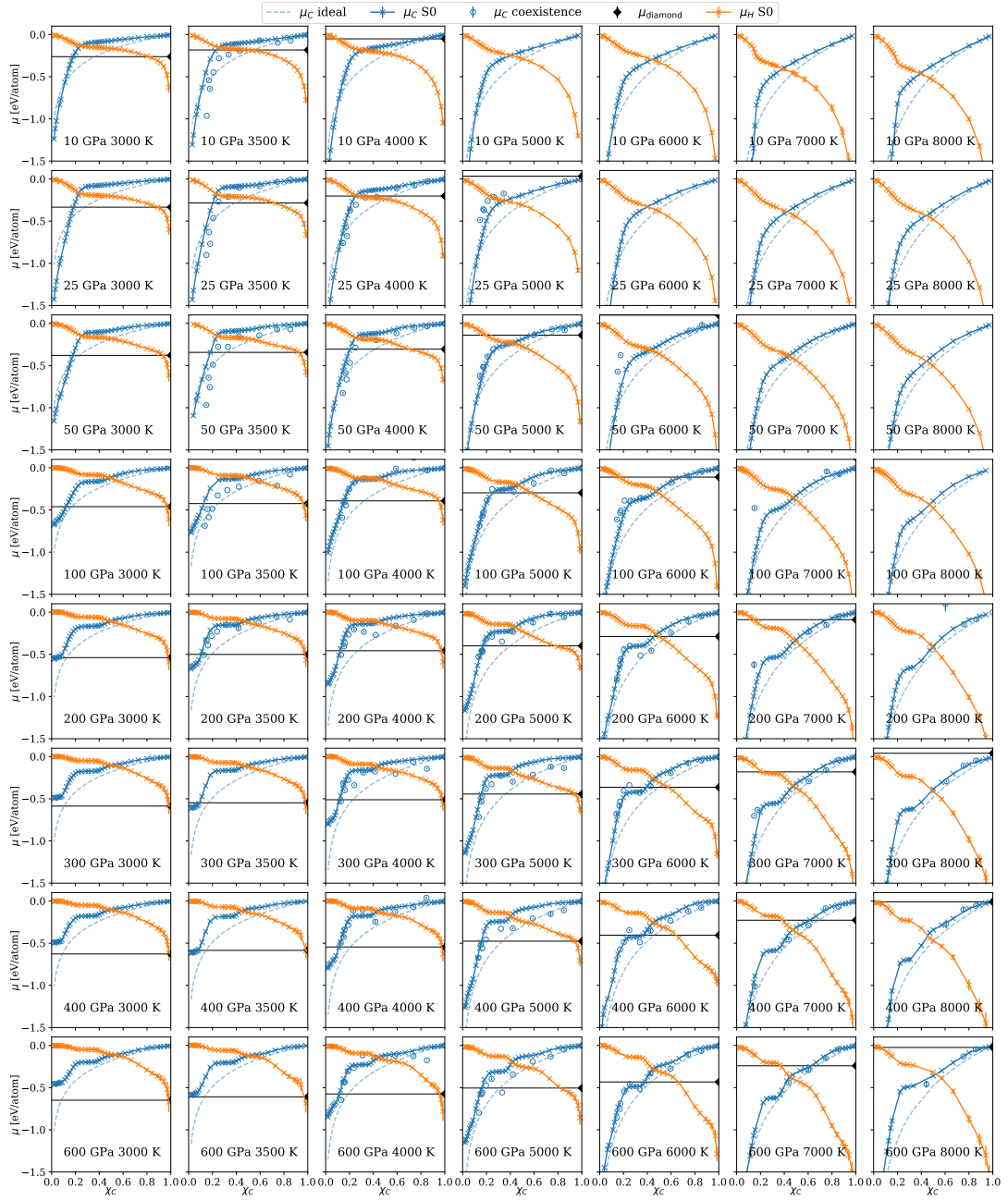


FIG. M4. The chemical potentials of carbon and hydrogen in C/H mixtures at different temperature and pressure conditions. The chemical potentials per carbon atom in C/H mixtures calculated using the S0 method are shown as blue crosses connected by solid curves, the values obtained using the coexistence method are shown as blue hollow symbols connected by dotted curves, and the ideal solution approximation is indicated by blue dashed curves. The chemical potentials per hydrogen atom calculated using the S0 method are shown as orange crosses. The chemical potential of diamond is indicated by the black diamond symbol and the black horizontal line.

- [1] H. E. Suess and H. C. Urey, “Abundances of the Elements,” *Rev. Mod. Phys.* **28**, 53 (1956).  
 [2] M. Mastrogiuseppe, V. Poggiali, A. G. Hayes, J. I. Lunine, R. Seu, G. Mitri, and R. D. Lorenz, “Deep and methane-rich lakes on Titan,” *Nat. Astron.* **3**, 535 (2019).  
 [3] T. Bertrand, F. Forget, B. Schmitt, O. L. White, and W. M.

- Grundy, “Equatorial mountains on Pluto are covered by methane frosts resulting from a unique atmospheric process,” *Nat. Commun.* **11**, 1 (2020).  
 [4] T. Guillot and D. Gautier, “10.16 - giant planets,” in *Treatise on Geophysics (Second Edition)*, edited by G. Schubert (2015) second edition ed., pp. 529–557.



- [5] N. Nettelmann, K. Wang, J. J. Fortney, S. Hamel, S. Yellamilli, M. Bethkenhagen, and R. Redmer, "Uranus evolution models with simple thermal boundary layers," *Icarus* **275**, 107 (2016).
- [6] P. G. J. Irwin, N. A. Teanby, D. Toledo, G. S. Orton, M. H. Wong, M. T. Roman, S. Pérez-Hoyos, A. James, and J. Dobinson, "Hazy blue worlds: A holistic aerosol model for Uranus and Neptune, including Dark Spots," *J. Geophys. Res. Planets* **127**, e2022JE007189 (2022).
- [7] R. Helled, M. Podolak, and E. Vos, "Methane planets and their mass-radius relation," *Astrophys. J. Lett.* **805**, L11 (2015).
- [8] M. Ross, "The ice layer in Uranus and Neptune—diamonds in the sky?" *Nature* **292**, 435 (1981).
- [9] J. C. Pearl and B. J. Conrath, "The albedo, effective temperature, and energy balance of Neptune, as determined from Voyager data," *J. Geophys. Res. Space Phys.* **96**, 18921 (1991).
- [10] P.-E. Tremblay, G. Fontaine, N. P. G. Fusillo, B. H. Dunlap, B. T. Gänsicke, M. A. Hollands, J. J. Hermes, T. R. Marsh, E. Cukanovaite, and T. Cunningham, "Core crystallization and pile-up in the cooling sequence of evolving white dwarfs," *Nature* **565**, 202 (2019).
- [11] L. R. Benedetti, J. H. Nguyen, W. A. Caldwell, H. Liu, M. Kruger, and R. Jeanloz, "Dissociation of CH<sub>4</sub> at high pressures and temperatures: diamond formation in giant planet interiors?" *Science* **286**, 100 (1999).
- [12] H. Hirai, K. Konagai, T. Kawamura, Y. Yamamoto, and T. Yagi, "Polymerization and diamond formation from melting methane and their implications in ice layer of giant planets," *Phys. Earth Planet. Inter.* **174**, 242 (2009).
- [13] S. S. Lobanov, P.-N. Chen, X.-J. Chen, C.-S. Zha, K. D. Litasov, H.-K. Mao, and A. F. Goncharov, "Carbon precipitation from heavy hydrocarbon fluid in deep planetary interiors," *Nat. Commun.* **4**, 2446 (2013).
- [14] H. Kadobayashi, S. Ohnishi, H. Ohfuji, Y. Yamamoto, M. Muraoka, S. Yoshida, N. Hirao, S. Kawaguchi-Imada, and H. Hirai, "Diamond formation from methane hydrate under the internal conditions of giant icy planets," *Sci. Rep.* **11**, 8165 (2021).
- [15] M. C. Marshall, M. G. Gorman, D. N. Polsin, J. H. Eggert, M. K. Ginnane, J. R. Rygg, G. W. Collins, and L. D. Leininger, "Diamond formation in double-shocked epoxy to 150 GPa," *J. Appl. Phys.* **131**, 085904 (2022).
- [16] D. Kraus, J. Vorberger, A. Pak, N. J. Hartley, L. B. Fletcher, S. Frydrych, E. Galtier, E. J. Gamboa, D. O. Gericke, S. H. Glenzer, E. Granados, M. J. MacDonald, A. J. MacKinnon, E. E. McBride, I. Nam, P. Neumayer, M. Roth, A. M. Saunders, A. K. Schuster, P. Sun, T. van Driel, T. Döppner, and R. W. Falcone, "Formation of diamonds in laser-compressed hydrocarbons at planetary interior conditions," *Nat. Astron.* **1**, 606 (2017).
- [17] N. J. Hartley, S. Brown, T. E. Cowan, E. Cunningham, T. Döppner, R. W. Falcone, L. B. Fletcher, S. Frydrych, E. Galtier, E. J. Gamboa, A. Laso Garcia, D. O. Gericke, S. H. Glenzer, E. Granados, P. A. Heimann, H. J. Lee, M. J. MacDonald, A. J. MacKinnon, E. E. McBride, I. Nam, P. Neumayer, A. Pak, A. Pelka, I. Prencipe, A. Ravasio, M. Rödel, K. Rohatsch, A. M. Saunders, M. Schölmerich, M. Schörner, A. K. Schuster, P. Sun, T. van Driel, J. Vorberger, and D. Kraus, "Evidence for crystalline structure in dynamically-compressed polyethylene up to 200 GPa," *Sci. Rep.* **9**, 4196 (2019).
- [18] G. Gao, A. R. Oganov, Y. Ma, H. Wang, P. Li, Y. Li, T. Iitaka, and G. Zou, "Dissociation of methane under high pressure," *J. Chem. Phys.* **133**, 144508 (2010).
- [19] A. S. Naumova, S. V. Lepeshkin, and A. R. Oganov, "Hydrocarbons under pressure: Phase diagrams and surprising new compounds in the c-h system," *J. Phys. Chem. C* **123**, 20497 (2019).
- [20] H. Liu, I. I. Naumov, and R. J. Hemley, "Dense hydrocarbon structures at megabar pressures," *J. Phys. Chem. Lett.* **7**, 4218 (2016).
- [21] L. J. Conway and A. Hermann, "High pressure hydrocarbons revisited: from van der Waals compounds to diamond," *Geosciences* **9**, 227 (2019).
- [22] T. Ishikawa and T. Miyake, "Evolutionary construction of a formation-energy convex hull: Practical scheme and application to a carbon-hydrogen binary system," *Phys. Rev. B* **101**, 214106 (2020).
- [23] F. Ancilotto, G. L. Chiarotti, S. Scandolo, and E. Tosatti, "Dissociation of methane into hydrocarbons at extreme (planetary) pressure and temperature," *Science* **275**, 1288 (1997).
- [24] B. L. Sherman, H. F. Wilson, D. Weeraratne, and B. Militzer, "Ab initio simulations of hot, dense methane during shock experiments," *Phys. Rev. B* **86**, 224113 (2012).
- [25] L. M. Ghiringhelli, C. Valeriani, E. J. Meijer, and D. Frenkel, "Local structure of liquid carbon controls diamond nucleation," *Phys. Rev. Lett.* **99**, 055702 (2007).
- [26] L. M. Ghiringhelli, J. H. Los, E. J. Meijer, A. Fasolino, and D. Frenkel, "Modeling the phase diagram of carbon," *Phys. Rev. Lett.* **94**, 145701 (2005).
- [27] X. Wang, S. Scandolo, and R. Car, "Carbon phase diagram from ab initio molecular dynamics," *Phys. Rev. Lett.* **95**, 185701 (2005).
- [28] A. A. Correa, S. A. Bonev, and G. Galli, "Carbon under extreme conditions: Phase boundaries and electronic properties from first-principles theory," *Proc. Natl. Acad. Sci. U. S. A.* **103**, 1204 (2006).
- [29] L. X. Benedict, K. P. Driver, S. Hamel, B. Militzer, T. Qi, A. A. Correa, A. Saul, and E. Schwegler, "Multiphase equation of state for carbon addressing high pressures and temperatures," *Phys. Rev. B* **89**, 224109 (2014).
- [30] J. H. Eggert, D. G. Hicks, P. M. Celliers, D. K. Bradley, R. S. McWilliams, R. Jeanloz, J. E. Miller, T. R. Boehly, and G. W. Collins, "Melting temperature of diamond at ultrahigh pressure," *Nat. Phys.* **6**, 40 (2010).
- [31] L. Scheibe, N. Nettelmann, and R. Redmer, "Thermal evolution of Uranus and Neptune," *Astronomy & Astrophysics* **632**, A70 (2019).
- [32] A. B. Zylstra, O. A. Hurricane, D. A. Callahan, A. L. Kritcher, J. E. Ralph, H. F. Robey, J. S. Ross, C. V. Young, K. L. Baker, D. T. Casey, T. Döppner, L. Divol, M. Hohenberger, S. Le Pape, A. Pak, P. K. Patel, R. Tommasini, S. J. Ali, P. A. Amendt, L. J. Atherton, B. Bachmann, D. Bailey, L. R. Benedetti, L. Berzak Hopkins, R. Betti, S. D. Bhandarkar, J. Biener, R. M. Bionta, N. W. Birge, E. J. Bond, D. K. Bradley, T. Braun, T. M. Briggs, M. W. Bruhn, P. M. Celliers, B. Chang, T. Chapman, H. Chen, C. Choate, A. R. Christopherson, D. S. Clark, J. W. Crippen, E. L. Dewald, T. R. Dittrich, M. J. Edwards, W. A. Farmer, J. E. Field, D. Fittinghoff, J. Frenje, J. Gaffney, M. Gatu Johnson, S. H. Glenzer, G. P. Grim, S. Haan, K. D. Hahn, G. N. Hall, B. A. Hammel, J. Harte, E. Hartouni, J. E. Heebner, V. J. Hernandez, H. Herrmann, M. C. Herrmann, D. E. Hinkel, D. D. Ho, J. P. Holder, W. W. Hsing, H. Huang, K. D. Humbird, N. Izumi, L. C. Jarrott, J. Jeet, O. Jones, G. D. Kerbel, S. M. Kerr, S. F. Khan, J. Kilkenny, Y. Kim, H. Geppert Kleinrath, V. Geppert Kleinrath, C. Kong, J. M. Koning, J. J. Kroll, M. K. G. Kruse, B. Kustowski, O. L. Landen, S. Langer, D. Larson, N. C. Lemos, J. D. Lindl, T. Ma, M. J. MacDonald, B. J. MacGowan, A. J. Mackinnon, S. A. MacLaren, A. G. MacPhee, M. M. Marinak, D. A. Mariscal, E. V. Marley, L. Masse, K. Meaney, N. B. Meezan, P. A. Michel, M. Millot, J. L. Milovich, J. D. Moody, A. S. Moore, J. W.

- Morton, T. Murphy, K. Newman, J. M. G. Di Nicola, A. Nikroo, R. Nora, M. V. Patel, L. J. Pelz, J. L. Peterson, Y. Ping, B. B. Pollock, M. Ratledge, N. G. Rice, H. Rinderknecht, M. Rosen, M. S. Rubery, J. D. Salmonson, J. Sater, S. Schiaffino, D. J. Schlossberg, M. B. Schneider, C. R. Schroeder, H. A. Scott, S. M. Sepke, K. Sequoia, M. W. Sherlock, S. Shin, V. A. Smalyuk, B. K. Spears, P. T. Springer, M. Stadermann, S. Stoupin, D. J. Strozzi, L. J. Suter, C. A. Thomas, R. P. J. Town, E. R. Tubman, C. Trosseille, P. L. Volegov, C. R. Weber, K. Widmann, C. Wild, C. H. Wilde, B. M. Van Wonterghem, D. T. Woods, B. N. Woodworth, M. Yamaguchi, S. T. Yang, and G. B. Zimmerman, "Burning plasma achieved in inertial fusion," *Nature* **601**, 542 (2022).
- [33] K. F. Kelton, "Crystal nucleation in liquids and glasses," in *Solid state physics*, Vol. 45 (Elsevier, 1991) pp. 75–177.
- [34] M. Volmer and A. Weber, "Keimbildung in übersättigten Gebilden," *Zeitschrift für physikalische Chemie* **119**, 277 (1926).
- [35] B. Cheng and M. Ceriotti, "Bridging the gap between atomistic and macroscopic models of homogeneous nucleation," *J. Chem. Phys.* **146**, 34106 (2017).
- [36] S. Auer and D. Frenkel, "Prediction of absolute crystal-nucleation rate in hard-sphere colloids," *Nature* **409**, 1020 (2001).
- [37] B. Cheng, C. Dellago, and M. Ceriotti, "Theoretical prediction of the homogeneous ice nucleation rate: Disentangling thermodynamics and kinetics," *Phys. Chem. Chem. Phys.* **20**, 28732 (2018).
- [38] R. Betti and O. A. Hurricane, "Inertial-confinement fusion with lasers," *Nat. Phys.* **12**, 435 (2016).
- [39] D. Frenkel, "Simulations: The dark side," *Eur. Phys. J. Plus* **128**, 10 (2013).
- [40] L. Li, T. Totton, and D. Frenkel, "Computational methodology for solubility prediction: Application to the sparingly soluble solutes," *J. Chem. Phys.* **146**, 214110 (2017).
- [41] B. Cheng, "Computing chemical potentials of solutions from structure factors," arXiv preprint arXiv:2205.03070 (2022).
- [42] P. R. ten Wolde and D. Frenkel, "Enhancement of protein crystal nucleation by critical density fluctuations," *Science* **277**, 1975 (1997).
- [43] R. Helled and J. J. Fortney, "The interiors of Uranus and Neptune: current understanding and open questions," *Philosophical Transactions of the Royal Society A* **378**, 20190474 (2020).
- [44] A. Vazan and R. Helled, "Explaining the low luminosity of Uranus: a self-consistent thermal and structural evolution," *Astron. Astrophys.* **633**, A50 (2020).
- [45] C. R. Mankovich and J. J. Fortney, "Evidence for a dichotomy in the interior structures of Jupiter and Saturn from helium phase separation," *Astrophys. J.* **889**, 51 (2020).
- [46] L. Zeng, S. B. Jacobsen, D. D. Sasselov, M. I. Petaev, A. Vanderburg, M. Lopez-Morales, J. Perez-Mercader, T. R. Mattsson, G. Li, M. Z. Heising, A. S. Bonomo, M. Damasso, T. A. Berger, H. Cao, A. Levi, and R. D. Wordsworth, "Growth model interpretation of planet size distribution," *Proc. Natl. Acad. Sci. U. S. A.* **116**, 9723 (2019).
- [47] G. Kresse and J. Hafner, "Ab initio molecular dynamics for liquid metals," *Phys. Rev. B* **47**, 558 (1993).
- [48] G. Kresse and J. Hafner, "Ab initio molecular dynamics for open-shell transition metals," *Phys. Rev. B* **48**, 13115 (1993).
- [49] G. Kresse and J. Hafner, "Ab initio molecular-dynamics simulation of the liquid-metal-amorphous-semiconductor transition in germanium," *Phys. Rev. B* **49**, 14251 (1994).
- [50] G. Kresse and J. Furthmüller, "Efficient iterative schemes for ab initio total-energy calculations using a plane-wave basis set," *Phys. Rev. B* **54**, 11169 (1996).
- [51] J. P. Perdew, K. Burke, and M. Ernzerhof, "Generalized gradient approximation made simple," *Phys. Rev. Lett.* **77**, 3865 (1996).
- [52] M. Bethkenhagen, E. R. Meyer, S. Hamel, N. Nettelmann, M. French, L. Scheibe, C. Ticknor, L. A. Collins, J. D. Kress, J. J. Fortney, and R. Redmer, "Planetary ices and the linear mixing approximation," *Astrophys. J.* **848**, 67 (2017).
- [53] B. Cheng, G. Mazzola, C. J. Pickard, and M. Ceriotti, "Evidence for supercritical behaviour of high-pressure liquid hydrogen," *Nature* **585**, 217 (2020).
- [54] J. Behler and M. Parrinello, "Generalized neural-network representation of high-dimensional potential-energy surfaces," *Phys. Rev. Lett.* **98**, 146401 (2007).
- [55] A. Singraber, T. Morawietz, J. Behler, and C. Dellago, "Parallel multistream training of high-dimensional neural network potentials," *Journal of Chemical Theory and Computation* **15**, 3075 (2019).
- [56] P. Rowe, V. L. Deringer, P. Gasparotto, G. Csányi, and A. Michaelides, "An accurate and transferable machine learning potential for carbon," *J. Chem. Phys.* **153**, 034702 (2020).
- [57] S. Plimpton, "Fast Parallel Algorithms for Short-Range Molecular Dynamics," *J. Comput. Phys.* **117**, 1 (1995).
- [58] A. Singraber, J. Behler, and C. Dellago, "Library-based LAMMPS implementation of high-dimensional neural network potentials," *J. Chem. Theory Comput.* **15**, 1827 (2019).
- [59] U. R. Pedersen, F. Hummel, G. Kresse, G. Kahl, and C. Dellago, "Computing gibbs free energy differences by interface pinning," *Phys. Rev. B* **88**, 94101 (2013).
- [60] G. A. Tribello, M. Bonomi, D. Branduardi, C. Camilloni, and G. Bussi, "Plumed 2: New feathers for an old bird," *Comput. Phys. Commun.* **185**, 604 (2014).
- [61] W. Lechner and C. Dellago, "Accurate determination of crystal structures based on averaged local bond order parameters," *J. Chem. Phys.* **129**, 114707 (2008).
- [62] P. J. Steinhardt, D. R. Nelson, and M. Ronchetti, "Bond-orientational order in liquids and glasses," *Physical Review B* **28**, 784 (1983).
- [63] B. Cheng and M. Ceriotti, "Computing the absolute Gibbs free energy in atomistic simulations: Applications to defects in solids," *Phys. Rev. B* **97**, 054102 (2018).
- [64] A. Reinhardt and B. Cheng, "Quantum-mechanical exploration of the phase diagram of water," *Nat. Commun.* **12**, 1 (2021).
- [65] A. Barducci, G. Bussi, and M. Parrinello, "Well-tempered metadynamics: a smoothly converging and tunable free-energy method," *Phys. Rev. Lett.* **100**, 20603 (2008).
- [66] D. Branduardi, G. Bussi, and M. Parrinello, "Metadynamics with adaptive gaussians," *J. Chem. Theory Comput.* **8**, 2247 (2012).

# Supplementary Information

## CONTENTS

I. Details on the DFT calculations	3
A. Convergence tests for DFT	3
B. Influence of the Fermi smearing	3
II. DFT MD calculations	5
III. Details on constructing the MLP	6
A. Training set	7
B. Training	8
C. Validation	8
IV. Benchmarks of the MLP	9
A. NVT simulation of pure liquid carbon	10
B. NVT simulation of diamond	12
C. NVT simulation of pure H	14
D. NVT simulation of CH <sub>4</sub>	16
E. NVT simulation of CH <sub>2</sub>	19
F. NVT simulation of C <sub>2</sub> H	23
G. Enthalpy of different solid carbon polymorphs	25
V. Simulations using the MLP	26
A. MLP MD simulations	26
B. NPT simulations of diamond and pure liquid carbon	26
C. Chemical potentials of pure carbon systems	27
D. Nucleation free energy of diamond from pure C liquid	28
E. Direct computation of the nucleation prefactor	31
F. Estimate of $f^+$ at other conditions	33
G. Chemical potential of C in C/H mixtures	33
H. Hydrocarbon crystals	33
VI. Carbon contents of planets and stars	35
A. Atmosphere	35

B. Neptune and Uranus interior models	36
C. White Dwarfs	36
References	37

## I. DETAILS ON THE DFT CALCULATIONS

We used the planewave code VASP [1–3] for production DFT calculations using the exchange-correlation functional by Perdew, Burke, and Ernzerhof (PBE) [4] and sampled the Brillouin zone using a k-point grid resolution of at least  $0.2 \text{ \AA}^{-1}$ . The planewave energy cutoff is set to 1000 eV and we used the C\_h and H\_h PBE projector augmented wave (PAW) potentials from the VASP library.

### A. Convergence tests for DFT

The convergence of our DFT calculations used for the evaluation of the training set was extensively tested. In particular, we paid close attention to the planewave energy cutoff and the k-point grid resolution, which are the most important parameters to ensure the targeted accuracy of the training set. We chose a diverse set of configurations to test both the planewave energy cutoff and the k-point grid resolution, including an isolated carbon atom, a carbon dimer, amorphous carbon between 3 and  $6.79 \text{ g/cm}^3$  and a high pressure phases of carbon (simple cubic). We also included liquid-like C/H structures with carbon concentrations of 0.008, 0.25, 0.67 and 0.89. The chosen configurations span the densities, pressure and stoichiometries of interest and have no electronic band gap hence they are particularly sensitive to the k-point grid resolution. We found that  $\Gamma$ -centered k-point grids with a "KSPACING" parameter of  $0.2 \text{ \AA}^{-1}$  are converged to better than 0.1% in pressure and 1 meV/atom in energy compared to a k-spacing of  $0.1 \text{ \AA}^{-1}$ . A planewave energy cutoff of 1000 eV is sufficient to reach 1% in pressure and 4 meV/atom in energy compared to 1500 eV calculations.

### B. Influence of the Fermi smearing

The forces in DFT are calculated based on the electronic free energy

$$F_{\text{el}} = E_{\text{el}} - T_{\text{el}}S_{\text{el}}, \quad (1)$$

where  $E_{\text{el}}$  and  $T_{\text{el}}$  are the internal energy and the temperature of the electrons, respectively. The Kohn-Sham electronic entropy  $S_{\text{el}}$  in the finite-temperature Fermi smearing approach is calculated according to

$$S_{\text{el}} = \sum_{nk} k_B (\ln(f_{nk}) + \ln(1 - f_{nk})), \quad (2)$$

where  $k_B$  is the Boltzmann constant and  $f_{nk}$  denotes the occupation number of each electronic band  $n$  at  $k$ -point  $k$  set according to the Fermi distribution:

$$f_{nk} = \frac{1}{\exp\left(\frac{\epsilon_{nk} - \mu}{k_B T_{\text{el}}} + 1\right)}, \quad (3)$$

where  $\mu$  is the electronic chemical potential and  $\epsilon_{nk}$  the energy of each state.  $T_{\text{el}}$  is the electronic temperature. In Fig. S1 we benchmark the change in forces as a function of carbon concentration and electronic temperature between 300 K and 9000 K. We calculate the root mean square deviation (RMSD) of the difference between the forces at  $T_{\text{el}} = T$  and  $T_{\text{el}} = 300$  K. We find that the effect is composition dependent in this range. The temperature dependence is small for temperatures below 4000 K (RMSD < 0.1 eV/Å) but becomes important at higher temperature: RMSD  $\sim$  0.3 eV/Å at 9000 K for pure carbon ( $\chi_C=1$ ). To take into account the impact of the thermal excitation of the electronic subsystem, for carbon and C/H mixtures we set  $T_{\text{el}}$  equal to the average ionic temperature during the DFT MD calculations as well as in the reference calculations used to train and test the MLP.

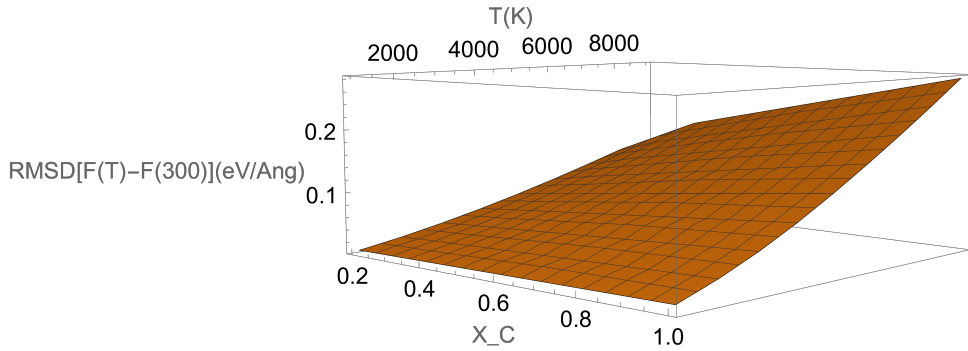


FIG. S1. Influence of the Fermi smearing on the forces at a pressure of about 300 GPa. We show here the root mean square deviation (RMSD) of the difference between the forces calculated using a Fermi smearing at a temperature  $T$  and at 300 K, as a function of temperature and for three compositions: C, CH<sub>2</sub> and CH<sub>4</sub>.

## II. DFT MD CALCULATIONS

We performed DFT molecular dynamics (DFT MD) simulations for the C/H system with various compositions to generate a variety of configurations to train the MLP and to create a data basis of thermodynamic, structural, and diffusive properties to benchmark our results obtained with the MLP. The DFT MD simulations were also performed with VASP [1–3] and used the same DFT parameters as described in section I except for the k-point sampling. The Brillouin zone was sampled at the Baldereschi Mean Value point, since MD runs typically require a less dense k-point grid [5]. The temperature was controlled using a Nosé-Hoover thermostat [6]. Further simulation parameters and considered thermodynamic conditions for each system are specified in the following.

*a. DFT MD of pure C liquid* This data set consists of simulations of 64 carbon atoms, starting from a liquid configuration, for temperatures between 6000 K and 10000 K and densities between  $3 \text{ g/cm}^3$  and  $8 \text{ g/cm}^3$  (every  $0.1 \text{ g/cm}^3$ ) yielding pressures between 45 GPa and 1474 GPa. The simulations were run with a timestep of 0.5 fs. The MD trajectories were generated using simulations lengths of at least 10 ps.

*b. DFT MD of diamond* A second data set for pure carbon was generated for the diamond phase. This data set also consists of simulations of 64 carbon atoms, this time starting from a solid (diamond) configuration for temperatures between 2000 K and 10000 K and densities between  $3.7 \text{ g/cm}^3$  and  $6.5 \text{ g/cm}^3$  (every  $0.2 \text{ g/cm}^3$ ). We also included a simulation at  $3.52 \text{ g/cm}^3$  and 300 K as well as simulations at  $6.889 \text{ g/cm}^3$  and temperatures between 6000 K and 10000 K. The pressure range spanned by these simulations is between 4 GPa and 1000 GPa. We used a timestep of 0.5 fs. The MD trajectories were generated using simulations lengths of at least 10 ps.

*c. DFT MD of  $\text{CH}_4$*  This data set is expanded based on earlier DFT MD calculations that primarily targeted the equation of state of high-pressure methane [7]. In total we considered 141 different density-temperature points, which we reanalyzed and partially extended in simulation length. The thermodynamic conditions cover densities between  $0.60 \text{ g/cm}^3$  and  $4.50 \text{ g/cm}^3$  yielding pressures between 3 GPa and 1440 GPa along 11 isotherms between 1000 K and 14000 K. The simulation cell contains 54 methane molecules that were initially placed on a bcc lattice. The simulations were run with a timestep of 0.25 fs. The MD trajectories were generated using simulations lengths of at least 10 ps.

*d. DFT MD of other C/H mixtures* We performed an extensive amount of DFT MD simulations for CH<sub>16</sub> (with 27 C and 432 H), CH<sub>8</sub> (with 36 C and 288 H), CH<sub>2</sub> (with 48 C and 96 H), CH (with 48 C and 48 H), C<sub>2</sub>H (with 48 C and 24 H), and C<sub>4</sub>H (with 64 C and 16 H) mixtures. The density grid was chosen to roughly cover a pressure range between 50 GPa and 600 GPa for each composition. We considered the following densities for CH<sub>16</sub>: 0.75 g/cm<sup>3</sup>, 1.05 g/cm<sup>3</sup>, 1.35 g/cm<sup>3</sup>, 1.65 g/cm<sup>3</sup>, 1.85 g/cm<sup>3</sup>, 2.15 g/cm<sup>3</sup>; for CH<sub>8</sub>: 0.95 g/cm<sup>3</sup>, 1.30 g/cm<sup>3</sup>, 1.70 g/cm<sup>3</sup>, 2.05 g/cm<sup>3</sup>, 2.30 g/cm<sup>3</sup>, 2.70 g/cm<sup>3</sup>; for CH: 2.30 g/cm<sup>3</sup>, 2.75 g/cm<sup>3</sup>, 3.35 g/cm<sup>3</sup>, 3.80 g/cm<sup>3</sup>, 4.20 g/cm<sup>3</sup>, 4.80 g/cm<sup>3</sup>; for CH<sub>2</sub>: 1.75 g/cm<sup>3</sup>, 2.20 g/cm<sup>3</sup>, 2.75 g/cm<sup>3</sup>, 3.25 g/cm<sup>3</sup>, 3.60 g/cm<sup>3</sup>, 4.15 g/cm<sup>3</sup>; for C<sub>2</sub>H: 2.65 g/cm<sup>3</sup>, 3.10 g/cm<sup>3</sup>, 3.75 g/cm<sup>3</sup>, 4.20 g/cm<sup>3</sup>, 4.60 g/cm<sup>3</sup>, 5.25 g/cm<sup>3</sup>; for C<sub>4</sub>H: 2.85 g/cm<sup>3</sup>, 3.40 g/cm<sup>3</sup>, 4.00 g/cm<sup>3</sup>, 4.50 g/cm<sup>3</sup>, 4.90 g/cm<sup>3</sup>, 5.60 g/cm<sup>3</sup>. For the carbon-rich mixtures C<sub>2</sub>H and C<sub>4</sub>H, we simulated the six different densities at 4000 K, 6000 K, and 8000 K; for all the other mixtures, we simulated six different densities at 3000 K, 4000 K, 6000 K, and 8000 K. All simulations were run for at least 7.5 ps at 8000 K and 12.5 ps for all other temperatures with a timestep size of 0.25 fs.

### III. DETAILS ON CONSTRUCTING THE MLP

To generate flexible and dissociable MLPs for high-pressure C/H mixtures, we employed an artificial neural network architecture built according to the framework of Behler and Parrinello [8], and used the N2P2 code [9]. In this framework, the total energy of the system is expressed as the sum of the individual contributions from atom-centered environments that encompass the relative coordinates of all neighboring atoms inside a cutoff radius. We used a cutoff radius of 10 Bohr. The same cutoff was also used for a previous MLP built for hydrogen, and a recent GAP model for carbon used 4.2Å [10] and 3.1Å [11]. To remove the rotational as well as the permutation variances of atomic coordinates, we selected 123 Behler-Parrinello symmetry functions (SFs) for carbon and 107 SFs for hydrogen atoms to describe the atomic environments, according to the correlations between the values of the SFs and the magnitude of forces on central atoms. The values of the SFs are then used as input vectors for the atomic neural networks that contain two hidden layers with 20 nodes each, yielding the atomic energy contributions. Finally, the total energy is a sum over the outputs of all individual atomic neural networks, and analytic gradients for the calculation of forces are readily available.

We constructed two versions of the MLPs (V1 and V2). V1 was used for all the production



simulations with carbon fractions  $\chi_C \geq 0.2$  ( $\text{CH}_4$  or more carbon-rich components), and V2 was used for all the other production simulations with  $\chi_C < 0.2$ . The behaviors of the two MLPs for systems with  $\chi_C \geq 0.2$  are very similar, but V2 is more accurate for dilute carbon solutions. Both versions of the MLPs are provided in the Supplementary Information.

### A. Training set

The training set for the MLP V1 has 84,657 configurations with a total of 7,133,531 atoms. For the MLP V2, the training set was expanded by including another 7,528 configurations with a total of 1,773,051 atoms.

*a. FPS selection from DFT MD simulations* The 6,490 most structurally diverse configurations were extracted from all the DFT MD trajectories of 54  $\text{CH}_4$  molecules using a farthest point sampling (FPS) algorithm. The ASAP code [12] was used in the visualization and the sparsification of the data set.

*b. High-pressure hydrogen* We added 48,679 snapshots of pure hydrogen configurations each with 8 to 128 atoms, which have previously served in training a recent MLP of pure hydrogen [13].

*c. Low and high-pressure carbon* We used all the carbon structures from the GAP20 data set [10], which contains 6,088 configurations with from 1 to 644 atoms. We also added 2,000 snapshots of pure liquid carbon configurations of 64 atoms selected using FPS from DFT MD trajectories, and another 2,000 solid structure of 72 or 108 atoms obtained from random searches and then adding small random displacements.

*d. Random searches* We included 17,500 structures with variable compositions generated using random crystal structure searches [14] using the AIRSS code employing different fits of the MLP. The system size of the structures in this set ranges from 32 to 254 atoms, and the simulation cell has either cubic or triclinic shapes.

*e. Active learning* We performed active learning in order to refine the training set. The snapshots of atomic positions were generated from replica exchange molecular dynamics runs at different temperatures. Subsequently, the structures with large variance of the predicted energies from 4 different fits of the MLP were selected. 1,900 structures each with 64-432 atoms of composition C, CH,  $\text{CH}_2$ ,  $\text{CH}_3$ ,  $\text{C}_2\text{H}$ ,  $\text{C}_3\text{H}$  were included this way.

*f. Extra structures for training MLP V2* To improve the description of the MLP for low carbon concentration mixtures, we used 7,528 structures with variable C/H ratios generated from MD simulations. This set was only used for training MLP V2.

## B. Training

For training the MLP V1, the resulting root mean squared errors (RMSE) of the energies in the training and test sets are 43 meV/atom and 42 meV/atom, respectively, and the RMSE values of the forces in the training and test sets are 865 meV/Å and 767 meV/Å, respectively.

For training the MLP V2, the RMSE of the energies in the training and test sets are 42 meV/atom and 45 meV/atom, respectively, and the RMSE values of the forces in the training and test sets are 922 meV/Å and 800 meV/Å, respectively.

## C. Validation

To validate the MLPs, we generated a very diverse set of C/H structures with variable compositions (73-380 total number of atoms in each configuration, carbon atomic fraction from about 1% to 94%). This set has a total of 3,884 structures, and was generated by running MLP NPT simulations at  $T = 2500$  K, 3000 K, 4000 K, 6000 K, and pressures between 10 GPa to 600 GPa. We then computed the PBE energies for these configurations and compared with the MLP energies, and the parity plot is shown in Fig. S2. For MLP V1, the resulting RMSE of the energies are 35 meV/atom, and the RMSE values of the forces are 827 meV/Å. For MLP V2, the resulting RMSE of the energies are 23 meV/atom, and the RMSE values of the forces are 807 meV/Å. These errors are smaller than the training/testing errors of the MLPs, meaning that both version of the MLPs can describe these diverse configurations extremely well. The MLP V2 is more accurate, which is due to a better description of the configurations with low carbon concentrations.

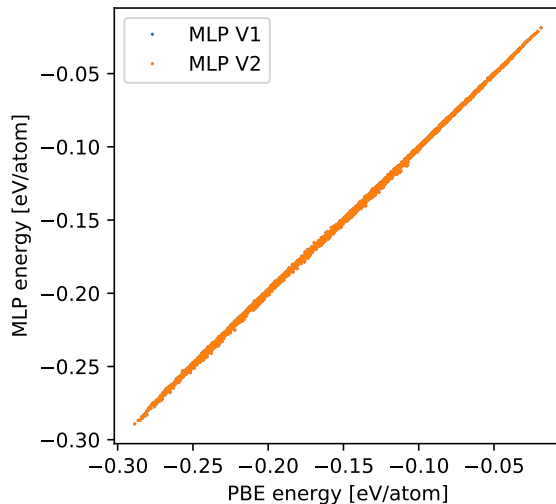


FIG. S2. A comparison between the MLP and the PBE energies for the structures in the validation set.

#### IV. BENCHMARKS OF THE MLP

We have performed extensive benchmarks of the MLP by comparing with DFT results based on the PBE exchange-correlation functional, including the comparison of equations of state (EOS), radial distribution functions, diffusion coefficients, and the enthalpies of solid structures. The details of the DFT MD simulations for pure carbon and methane are provided in Sec. II, and the DFT MD results for pure hydrogen were taken from Ref. [13]. The NVT simulations using the MLP were carried out using LAMMPS [15] interfaced with N2P2 [16]. The simulation setup of the MLP MD was selected to closely resemble the DFT MD runs: same initial configurations, same thermodynamic conditions, same time step size and simulation length. This section provides the detailed benchmark data.

We performed the benchmark based on the systems of liquid carbon, diamond, liquid hydrogen,  $\text{CH}_{16}$ ,  $\text{CH}_8$ ,  $\text{CH}_4$ ,  $\text{CH}_2$ ,  $\text{CH}$ ,  $\text{C}_2\text{H}$ , and  $\text{C}_4\text{H}$  mixtures. For all these systems, we covered a wide range of temperature and pressure conditions (50 GPa-600 GPa and beyond). Here we present the benchmark of liquid carbon, diamond, liquid hydrogen,  $\text{CH}_4$ ,  $\text{CH}_2$ , and  $\text{C}_2\text{H}$ , and the rest of the benchmark is provided in the SI repository.

### A. NVT simulation of pure liquid carbon

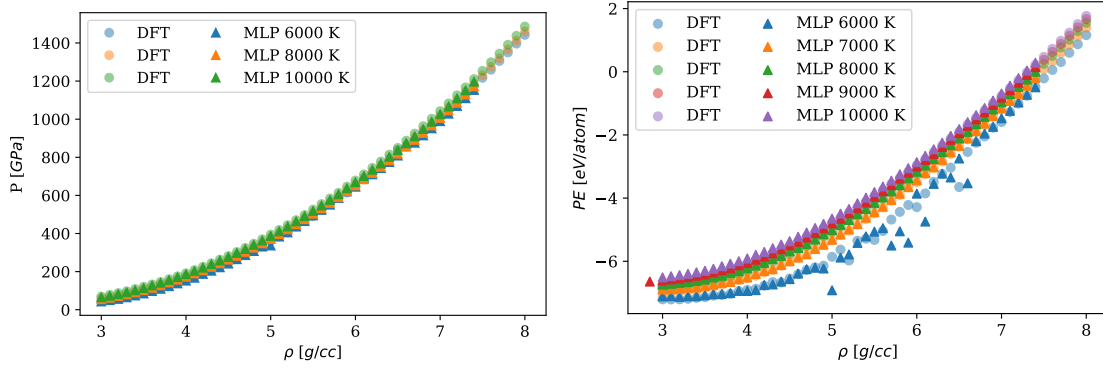


FIG. S3. Pressure (left panel) and potential energy (right panel) of pure liquid carbon computed from equilibrium MD simulations in the NVT ensemble with a system size of 64 carbon atoms. The solid triangular symbols are the results from the MLP, and the semi-transparent circles are from PBE DFT.

The MLP MD data set consists of simulations of 64 carbon atoms starting from a liquid configuration for temperatures between 6000 K and 10000 K and densities between  $3.3 \text{ g/cm}^3$  and  $7.3 \text{ g/cm}^3$ , yielding pressures between about 45 GPa and 1100 GPa. Fig. S3 compares the liquid carbon EOS obtained from the MLP and the DFT NVT simulations, while Fig. S4 shows the respective carbon-carbon radial distribution functions. Overall, the comparison between the MLP and PBE DFT simulations is good, the only exception is a noticeable difference for some densities at 6000 K, which is due to the different onset of solidification.

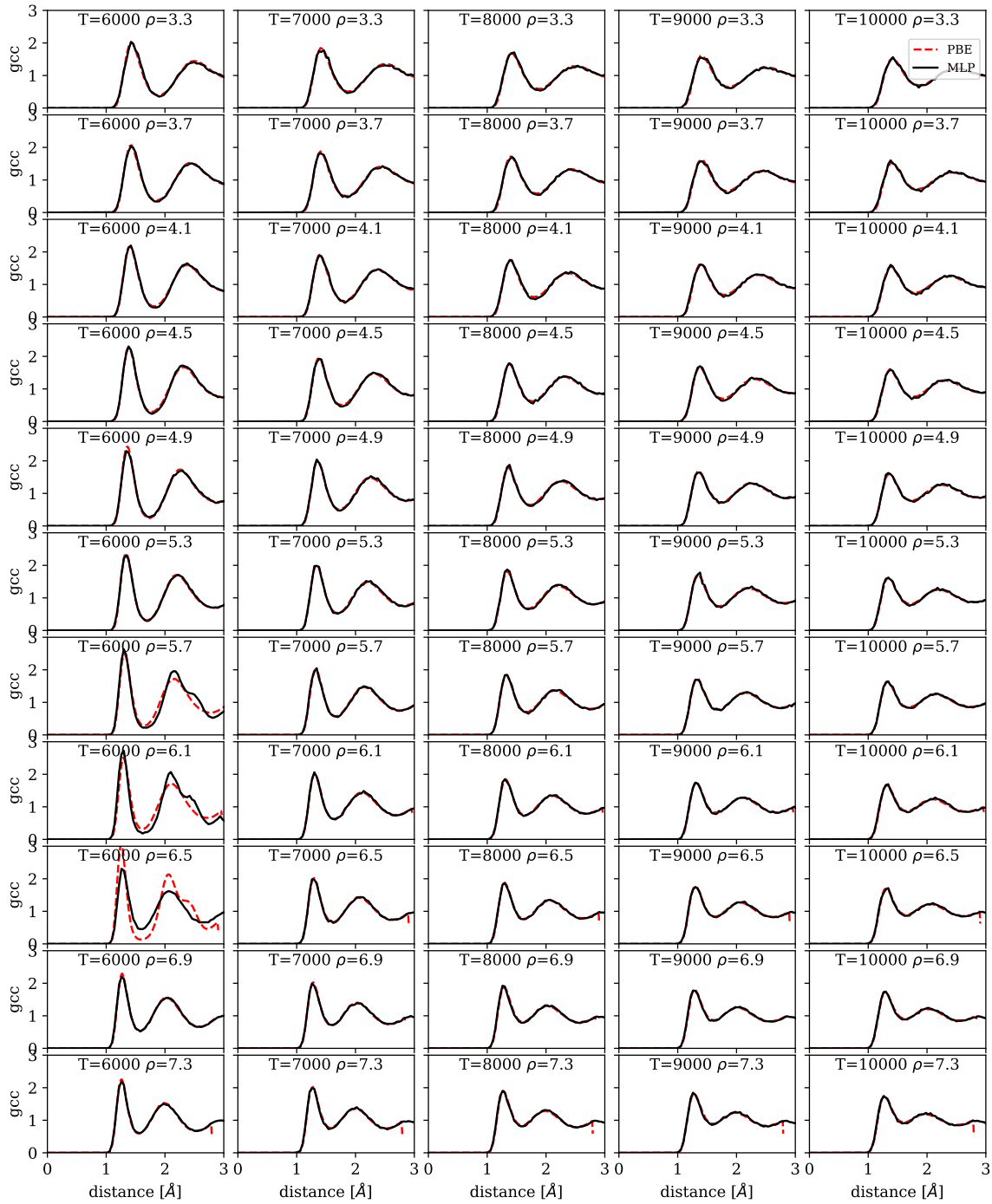


FIG. S4. Carbon-carbon radial distribution functions  $g_{cc}$  of pure liquid carbon computed from equilibrium MD simulations in the NVT ensemble with a system size of 64 carbon atoms. The solid black lines are the results from the MLP, and the dashed red lines are from PBE DFT.

## B. NVT simulation of diamond

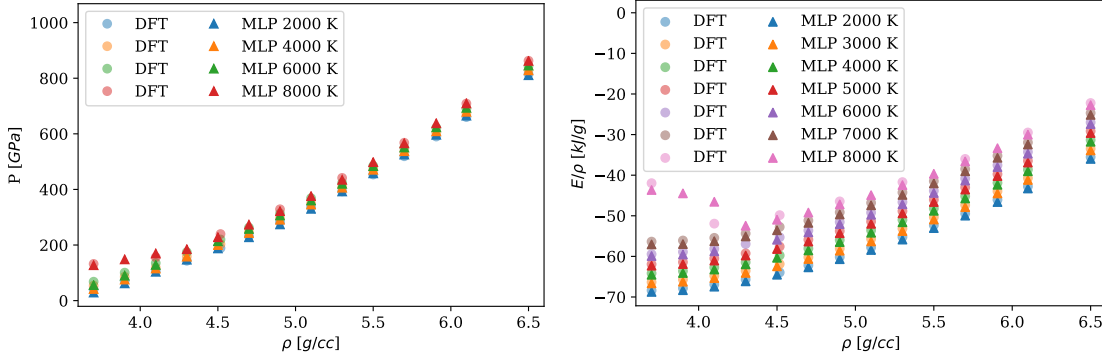


FIG. S5. Pressure (left panel) and equilibrium energy per unit mass ( $E/\rho$ ) (right panel) of pure diamond computed from equilibrium molecular dynamics simulations in the NVT ensemble with a system size of 64 carbon atoms. The solid triangular symbols are the results from the MLP, and the semi-transparent circles are from PBE DFT.

This data set consists of simulations of 64 carbon atoms, starting from a diamond configuration for temperatures between 2000 K and 8000 K and densities between  $3.7 \text{ g/cm}^3$  and  $6.5 \text{ g/cm}^3$ , yielding pressures between 40 GPa and 1000 GPa. Fig. S5 shows the comparison of EOS from the MLP and the PBE DFT NVT simulations. Both DFT MD and MLP MD simulations of diamond at 8000 K and low densities have melted, with a different onset of melting time during the MD runs. Fig. S6 shows the benchmark results for the C-C radial distribution functions.



FIG. S6. Carbon-carbon radial distribution functions  $g_{cc}$  of pure diamond computed from equilibrium MD simulations at the NVT ensemble with a system size of 64 carbon atoms. The solid black lines are the results from the MLP, and the dashed red lines are from PBE DFT.

### C. NVT simulation of pure H

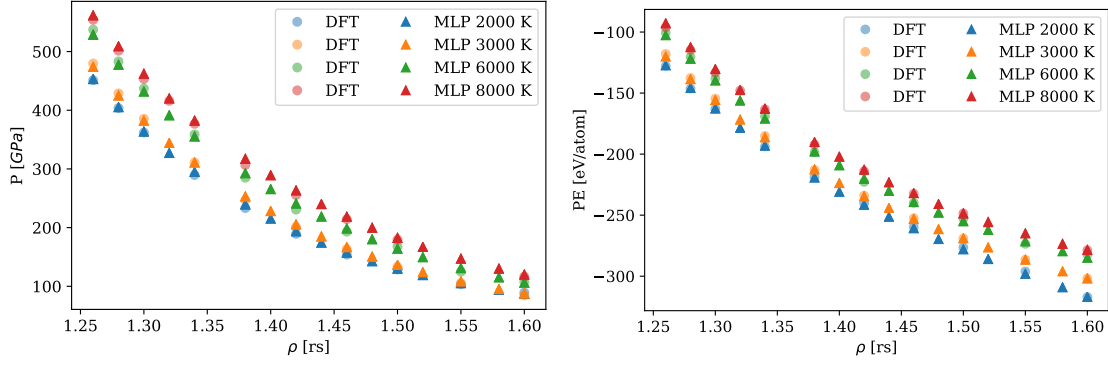


FIG. S7. Pressure (left panel) and potential energy (right panel) of pure liquid hydrogen computed from equilibrium MD simulations in the NVT ensemble with a system size of 128 hydrogen atoms. The solid triangular symbols are the results from the MLP, and the semi-transparent circles are from PBE DFT.

The PBE DFT simulations at the NVT ensemble were taken from Ref. [13]. The densities ranging from  $r_s = 1.26$  to  $r_s = 1.60$  (i.e. 1.348-0.658 g/mL), correspond to a pressure range of about 80 GPa to 550 GPa. The density is expressed in terms of the Wigner-Seitz radius  $r_s$ , as customary in the studies of high-pressure hydrogen.  $r_s$  is the radius of a sphere whose volume is equal to the volume per atom in the units of the Bohr radius. The density in this unit can be converted to g/mL via the relationship  $\rho[\text{g/mL}] = 2.6966/(\rho[r_s])^3$ . The system size is 128 H atoms. We considered temperatures between 2000 K and 8000 K. Fig. S7 shows the comparison of EOS from the MLP and the PBE DFT NVT simulations and Fig. S8 shows the H-H radial distribution functions.



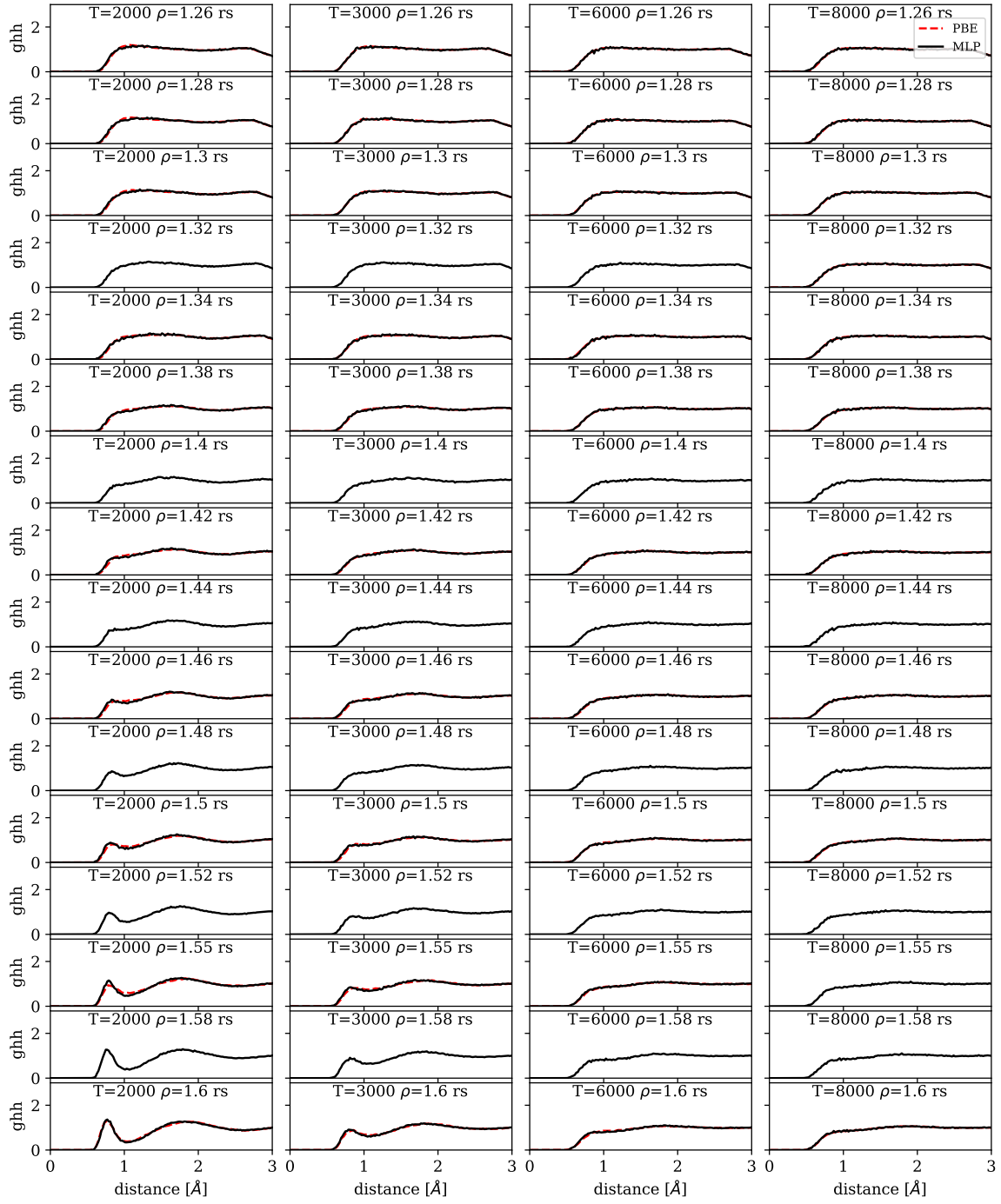


FIG. S8. Hydrogen-hydrogen radial distribution functions  $ghh$  of pure hydrogen system computed from equilibrium MD simulations at the NVT ensemble with a system size of 128 hydrogen atoms. The solid black lines are the results from the MLP, and the dashed red lines are from PBE DFT.

#### D. NVT simulation of CH<sub>4</sub>

We performed NVT simulations for systems of 54 CH<sub>4</sub> molecules using the MLP. The initial configuration has 54 methane molecules with ordered orientations placed on a bcc lattice. The equations of state and the diffusion coefficients are plotted in Fig. S9. The C-C, C-H and H-H radial distribution functions are plotted in Fig. S10, Fig. S11, and Fig. S12, respectively. The thermodynamic conditions cover densities between 0.60 g/cm<sup>3</sup> and 4.50 g/cm<sup>3</sup>, and temperatures between 1000 K and 8000 K, corresponding to pressures between about 20 GPa and 1300 GPa. At  $T = 3000$  K,  $\rho = 1.5$  g/cm<sup>3</sup>, the CH<sub>4</sub> system in DFT MD remain bcc, but has melted in the MLP MD simulation. The results also differ significantly at 4.50 g/cm<sup>3</sup> translating to pressures higher than 1000 GPa, which we do not consider in the present study.

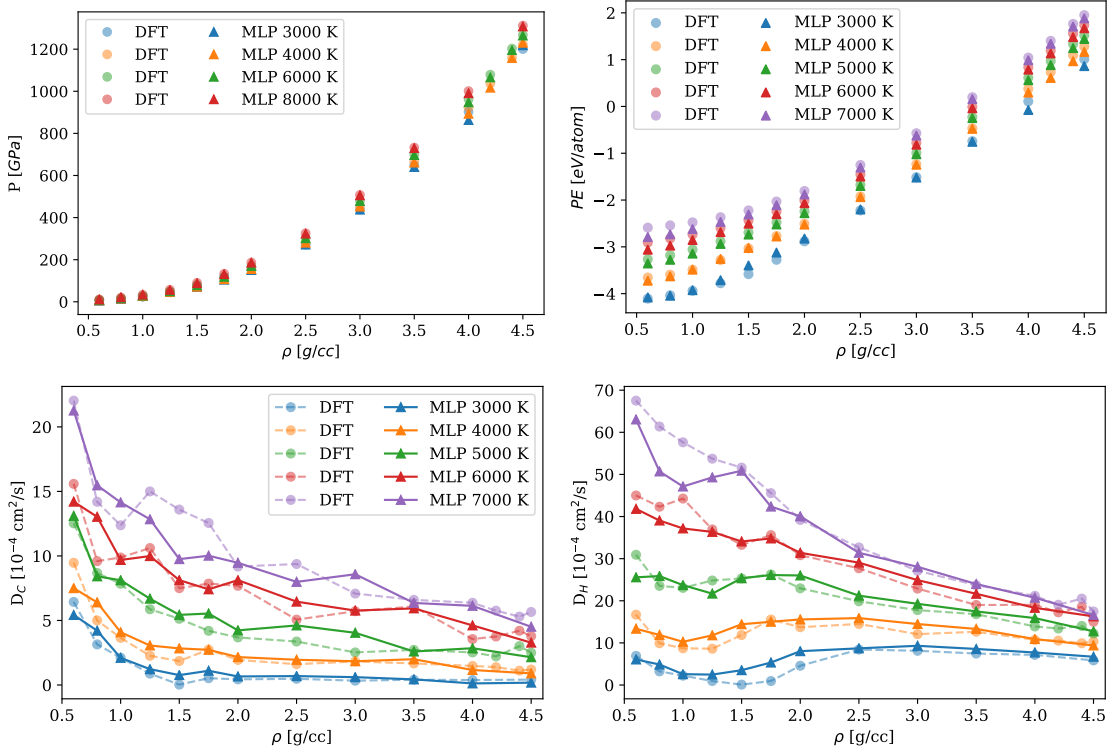


FIG. S9. Comparison between the potential energy (PE), pressure ( $P$ ), the diffusion coefficient of hydrogen ( $D_H$ ), and the diffusion coefficient of carbon ( $D_C$ ), predicted by PBE DFT and the MLP. The results are from MD simulations of 54 CH<sub>4</sub> molecules in the NVT ensemble.

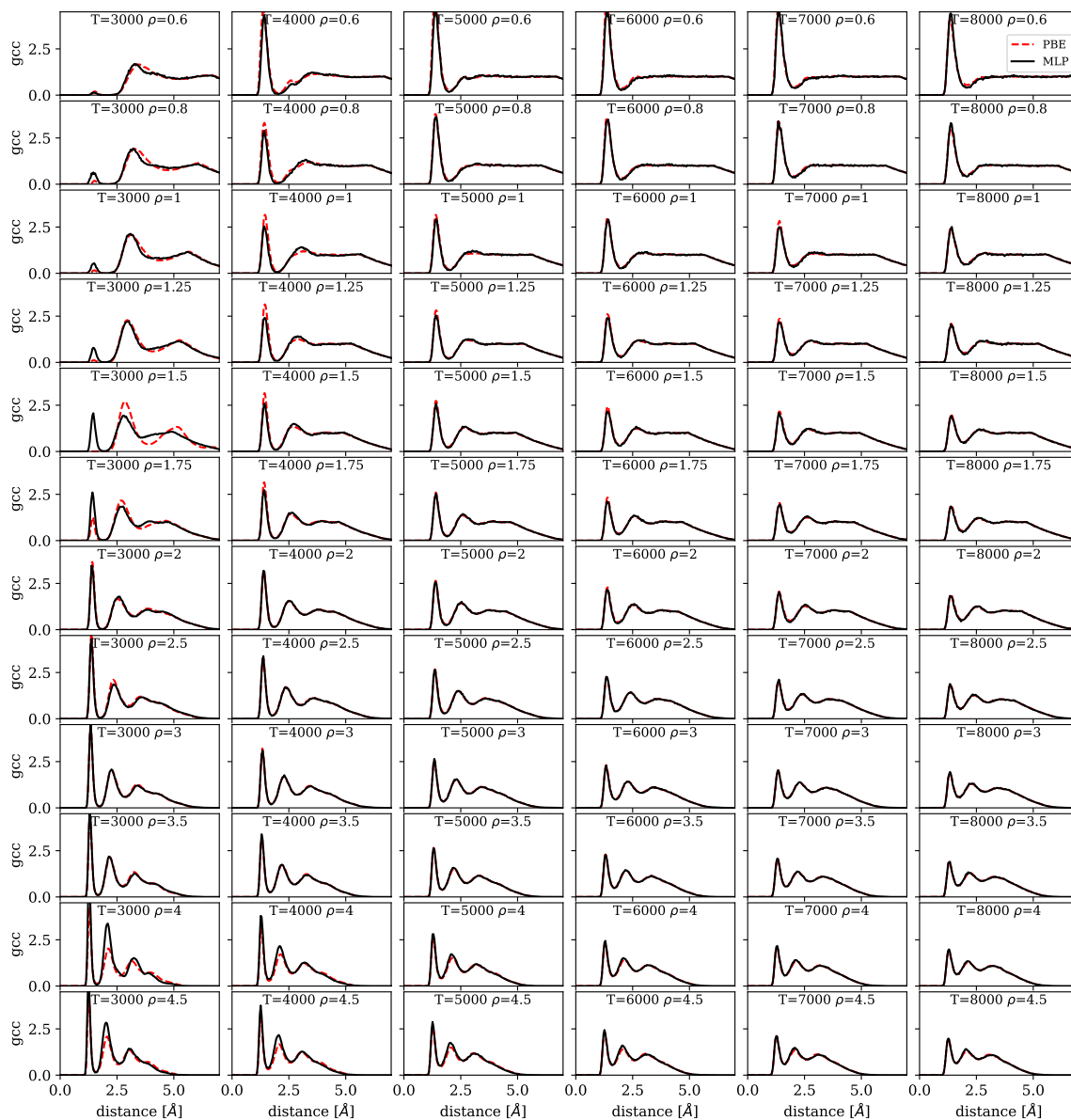


FIG. S10. Carbon-carbon radial distribution functions  $g_{cc}$  of methane computed from equilibrium MD simulations in the NVT ensemble with a system size of 54  $\text{CH}_4$  formula units. The solid black lines are the results from the MLP, and the dashed red lines are from PBE DFT.

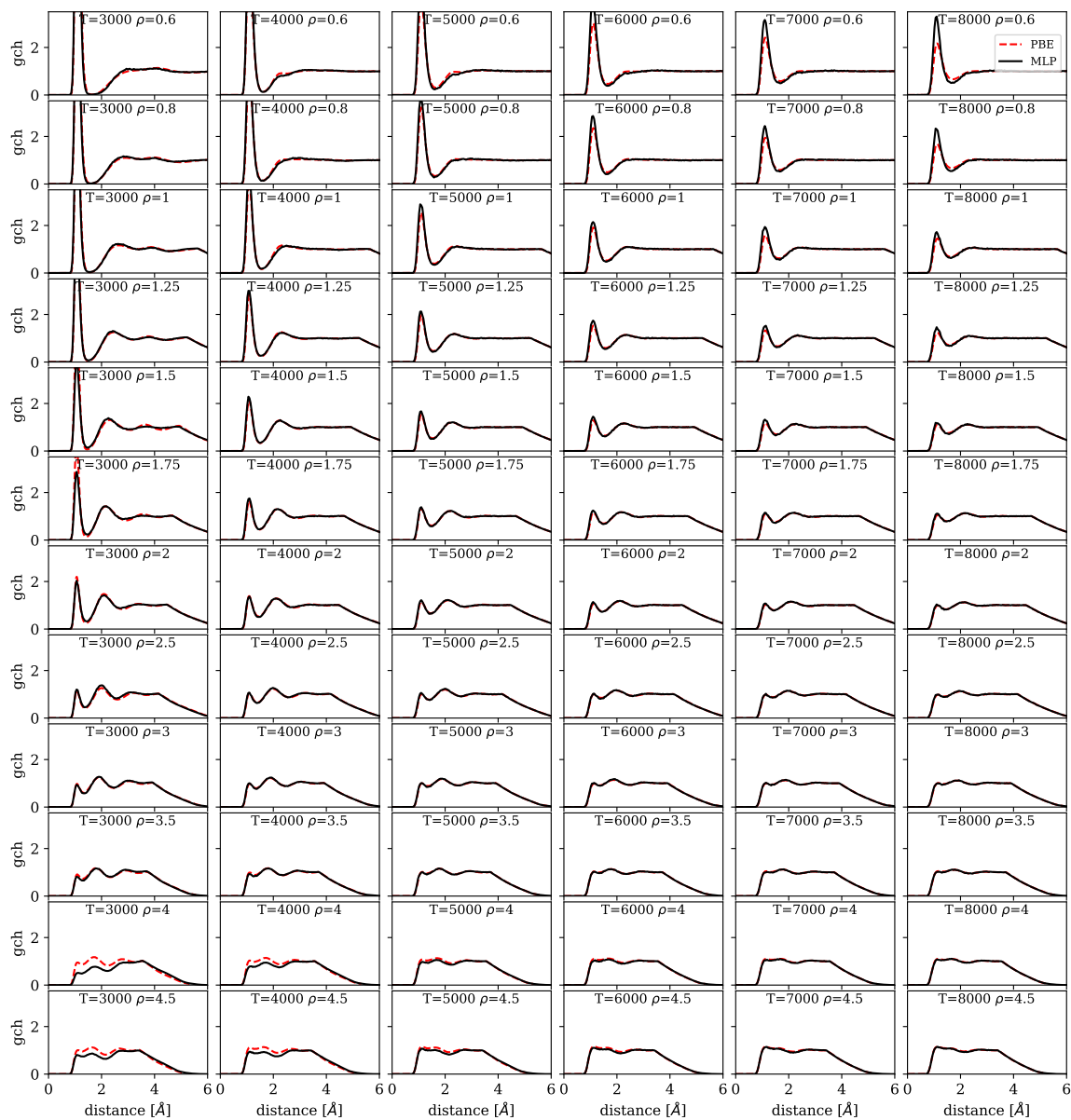


FIG. S11. Carbon-hydrogen radial distribution functions  $g_{ch}$  of methane computed from equilibrium MD simulations at the NVT ensemble with a system size of 54  $\text{CH}_4$  formula units. The solid black lines are the results from the MLP, and the dashed red lines are from PBE DFT.

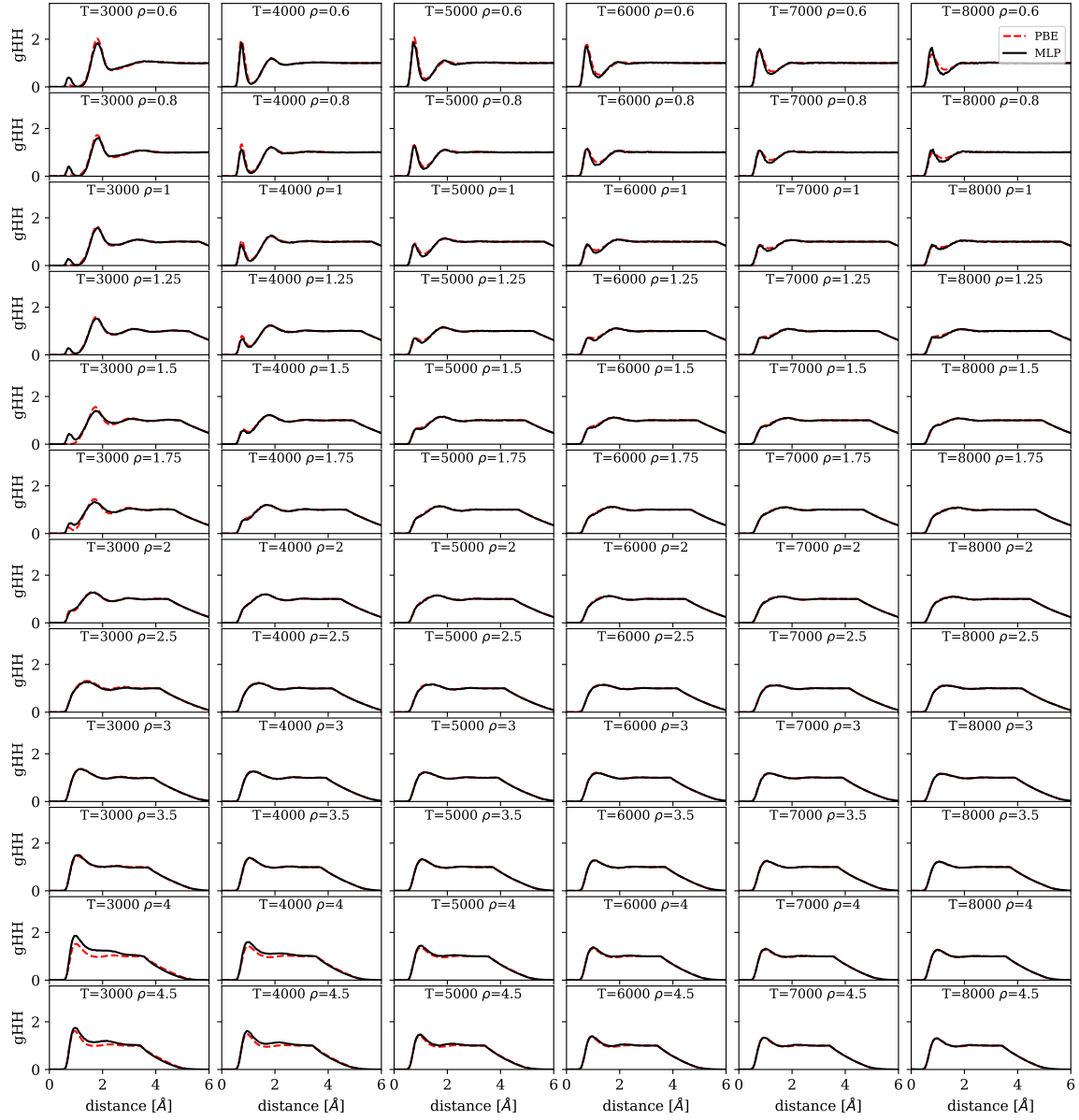


FIG. S12. Hydrogen-hydrogen radial distribution functions  $g_{HH}$  of methane computed from equilibrium MD simulations at the NVT ensemble with a system size of 54  $\text{CH}_4$  formula units. The solid black lines are the results from the MLP, and the dashed red lines are from PBE DFT.

### E. NVT simulation of $\text{CH}_2$

We performed NVT simulations for systems of 48  $\text{CH}_2$  molecules using the MLP. The initial configuration resembles an amorphous structure. The equations of state are plotted in Fig. S13.

The C-C, C-H and H-H radial distribution functions are plotted in Fig. S14, Fig. S15, and Fig. S16, respectively.

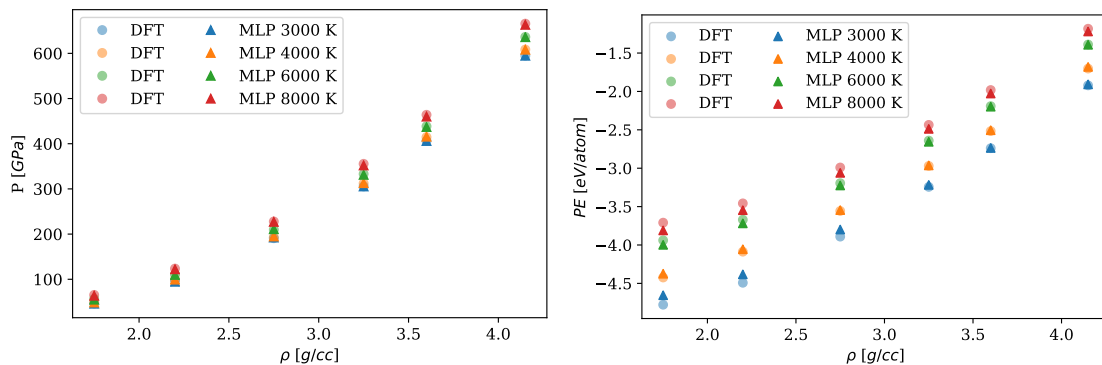


FIG. S13. Comparison between the potential energy (PE) and pressure ( $P$ ) predicted by PBE DFT and the MLP. The results are from MD simulations of 48 CH<sub>2</sub> molecules in the NVT ensemble.

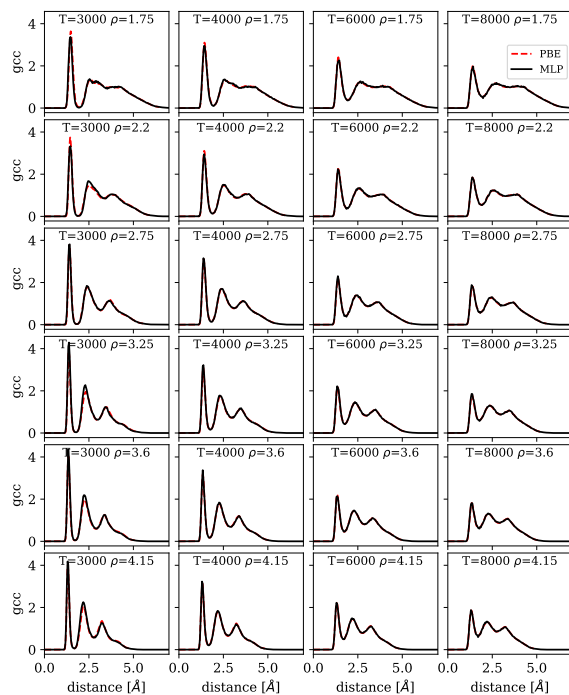


FIG. S14. Carbon-carbon radial distribution functions  $g_{cc}$  of CH<sub>2</sub> computed from equilibrium MD simulations in the NVT ensemble with a system size of 48 CH<sub>2</sub> formula units. The solid black lines are the results from the MLP, and the dashed red lines are from PBE DFT.

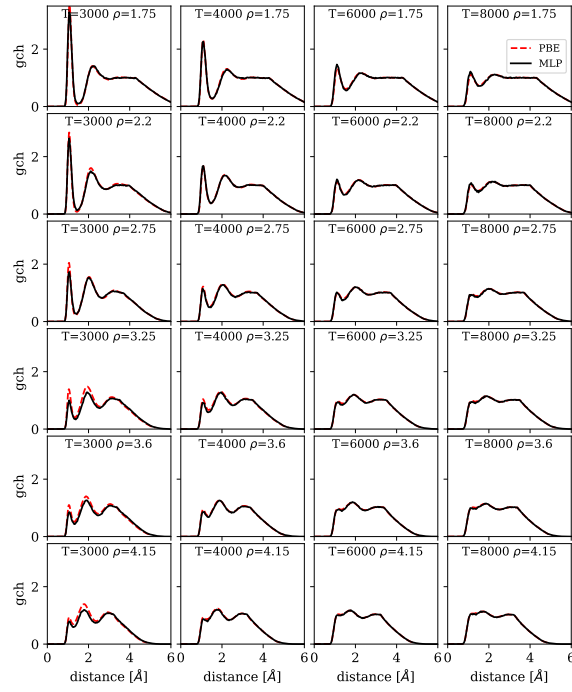


FIG. S15. Carbon-hydrogen radial distribution functions  $g_{ch}$  of  $\text{CH}_2$  computed from equilibrium MD simulations at the NVT ensemble with a system size of 48  $\text{CH}_2$  formula units. The solid black lines are the results from the MLP, and the dashed red lines are from PBE DFT.

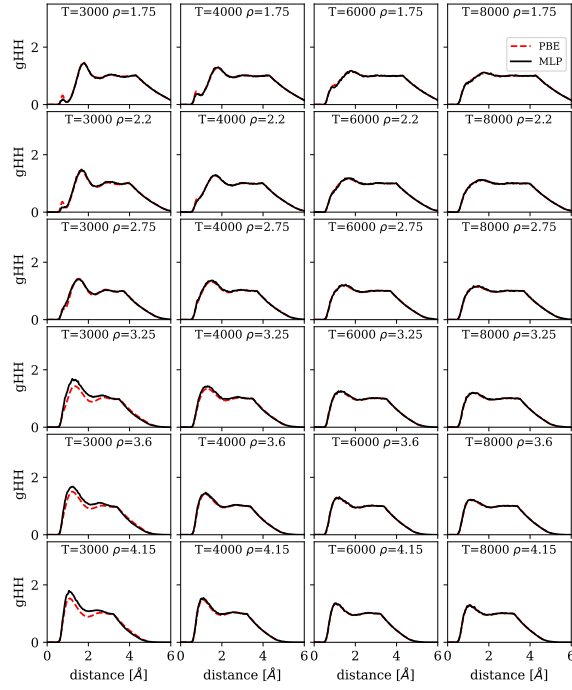


FIG. S16. Hydrogen-hydrogen radial distribution functions  $g_{HH}$  of  $\text{CH}_2$  computed from equilibrium MD simulations at the NVT ensemble with a system size of 48  $\text{CH}_2$  formula units. The solid black lines are the results from the MLP, and the dashed red lines are from PBE DFT.



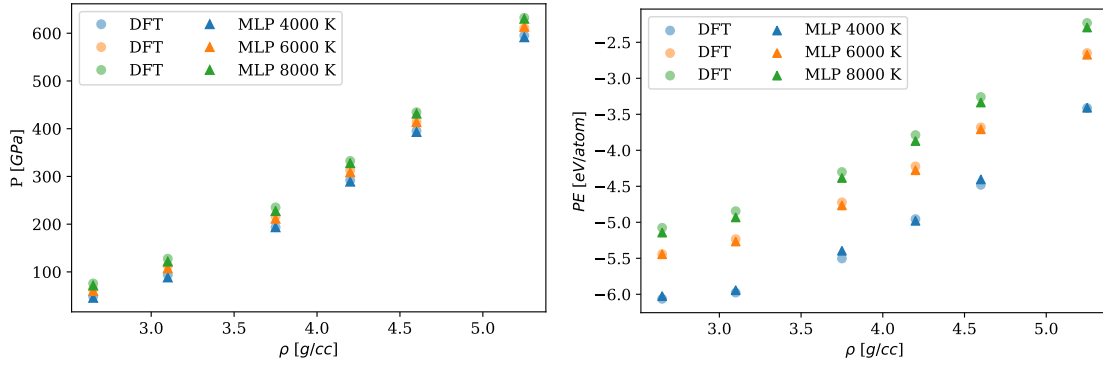


FIG. S17. Comparison between the potential energy (PE) and pressure ( $P$ ) predicted by PBE DFT and the MLP. The results are from MD simulations of 24  $C_2H$  molecules in the NVT ensemble.

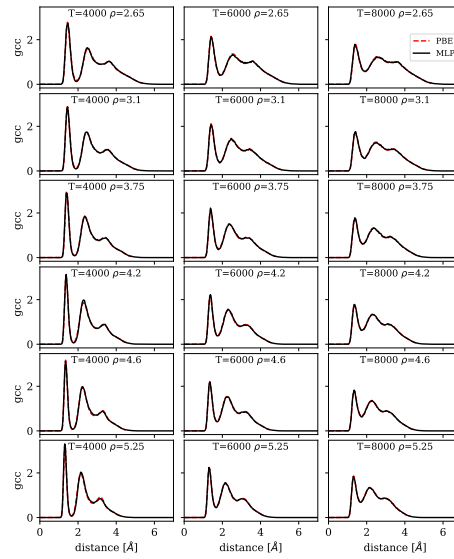


FIG. S18. Carbon-carbon radial distribution functions  $g_{cc}$  of  $CH_2$  computed from equilibrium MD simulations in the NVT ensemble with a system size of 24  $C_2H$  formula units. The solid black lines are the results from the MLP, and the dashed red lines are from PBE DFT.

## F. NVT simulation of $C_2H$

We performed NVT simulations for systems of 24  $C_2H$  molecules using the MLP. The initial configuration resembles an amorphous structure. The equations of state are plotted in Fig. S17. The C-C, C-H and H-H radial distribution functions are plotted in Fig. S18, Fig. S19, and Fig. S20, respectively.

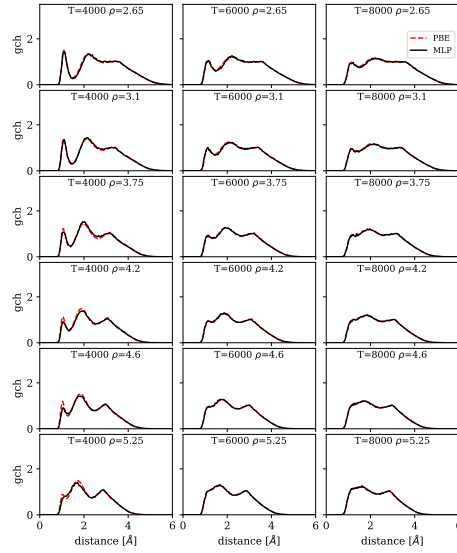


FIG. S19. Carbon-hydrogen radial distribution functions  $g_{ch}$  of  $C_2H$  computed from equilibrium MD simulations at the NVT ensemble with a system size of 24  $C_2H$  formula units. The solid black lines are the results from the MLP, and the dashed red lines are from PBE DFT.

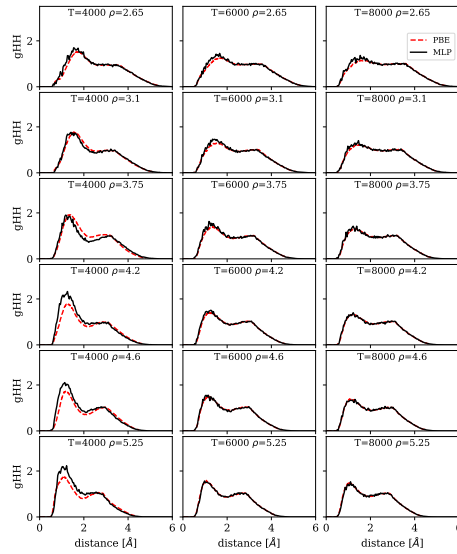


FIG. S20. Hydrogen-hydrogen radial distribution functions  $g_{hh}$  of  $C_2H$  computed from equilibrium MD simulations at the NVT ensemble with a system size of 24  $C_2H$  formula units. The solid black lines are the results from the MLP, and the dashed red lines are from PBE DFT.

### G. Enthalpy of different solid carbon polymorphs

We first performed random structure searches [14] using the MLP to find low-energy solid carbon polymorphs. Using these polymorphs, we computed the 0 K enthalpy at pressures from 0 to 900 GPa, employing both the MLP and PBE DFT. The results are shown in Fig. S21. The Fddd phase is graphite, while the Fd3m, R3m, and P63mmc phases are diamond structures with different stacking sequences. Ia3 structure is also often referred to as BC8 carbon.

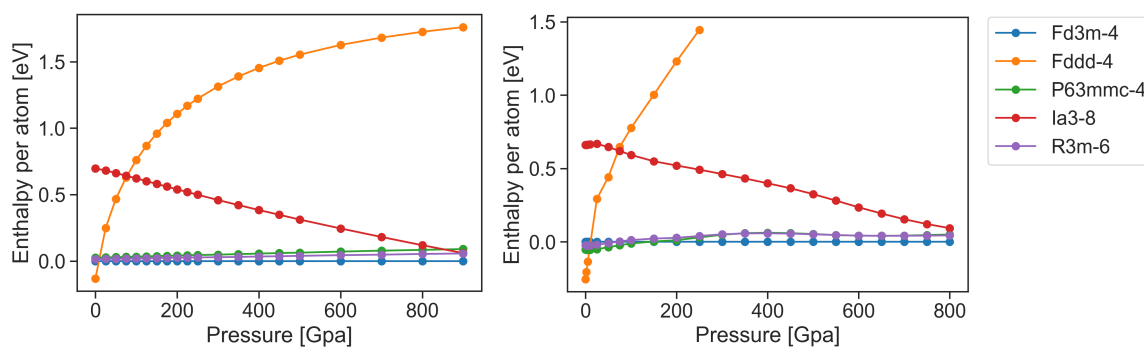


FIG. S21. 0 K enthalpy curves for different solid carbon phases. The left is from PBE DFT, and the right is from MLP.

## V. SIMULATIONS USING THE MLP

### A. MLP MD simulations

All MLP MD simulations were performed in LAMMPS [15] with a neural network potential implementation [16]. The simulations of the bulk phases were performed in the NPT ensemble using the Nosé-Hoover isotropic barostat. The time step size was chosen to 0.25 fs for C/H mixtures, 0.4 fs for pure carbon, and 0.2 fs for pure hydrogen.

### B. NPT simulations of diamond and pure liquid carbon

A series of NPT simulations was performed at 2500 K to 10000 K and 10 GPa to 600 GPa for diamond and pure liquid carbon phases. The system size was 512 carbon atoms. The simulation time was 120 ps. Besides computing the EOS, we collected the diffusion coefficient of carbon in the bulk liquid (Fig. S22).

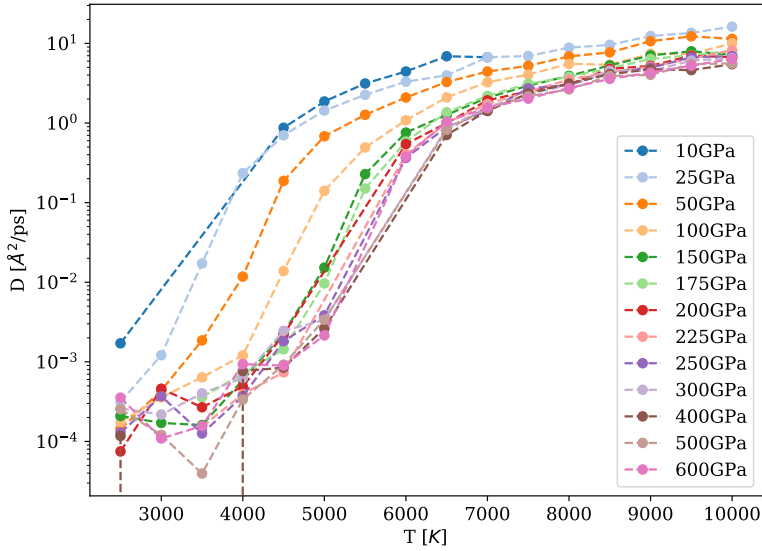


FIG. S22. Diffusion coefficient of carbon in the bulk liquid computed using the MLP in the NPT ensemble.

### C. Chemical potentials of pure carbon systems

To compute  $\Delta\mu_D$ , interface pinning simulations [17] were performed using the PLUMED code [18] on a diamond-liquid carbon system containing 1,024 carbon atoms at pressures between 0 GPa and 800 GPa employing the MLP. The simulation length was 80 ps after equilibration. A Nosé-Hoover barostat was only applied along the  $z$  direction, which is perpendicular to the interface in the coexistence simulations. The dimensions of the supercell along  $x$  and  $y$  directions were commensurate with the equilibrium lattice parameters of the diamond phase at the given conditions. An umbrella potential with stiffness  $\alpha$  was added to the Hamiltonian of the system:

$$\mathcal{H}_{biased}(\mathbf{q}) = \mathcal{H}(\mathbf{q}) + \frac{\alpha}{2} (\Phi - \bar{\Phi})^2, \quad (4)$$

where  $\Phi = \sum_{i=1}^N \phi_i$  is an extensive collective variable (CV) of the whole system that is constructed by summing up the order parameters  $\phi_i$  of each carbon atom. More specifically, we used a locally-averaged [19]  $Q_3$  order parameter [20] as atom-centered order parameter for detecting diamond structures, which we transformed with a hyperbolic switching function to enhance its resolution capability between solid and liquid-like atomic environments [21]. The relevant part of the PLUMED input files that contain the specification of the order parameters are:

```
Q3 ...
LABEL=q3
SPECIES=1-1024 SWITCH={CUBIC D_0=1.6 D_MAX=1.8}
MEAN
LOWMEM
... Q3

LOCAL_AVERAGE ...
LABEL=m3
SPECIES=q3
SWITCH={CUBIC D_0=1.6 D_MAX=1.8}
MEAN
MORE_THAN1={SMAP R_0=0.05 D_0=0.2 A=8 B=8}
LOWMEM
... LOCAL_AVERAGE
```

```
# apply the umbrella potential
RESTRAINT ARG=m3.morethan-1 AT=250 KAPPA=1.0 LABEL=res
```

Finally, the difference in chemical potential per atom between the diamond and the liquid carbon phases in the simulations can be computed using

$$\Delta\mu_D = \mu_{diamond} - \mu_{liquidC} = \alpha \frac{\bar{\Phi} - \langle\Phi\rangle}{\langle\phi\rangle_{diamond} - \langle\phi\rangle_{liquidC}}, \quad (5)$$

where  $\langle\Phi\rangle$  is the average order parameter from the interface pinning simulations, and  $\langle\phi\rangle_{diamond}$  and  $\langle\phi\rangle_{liquidC}$  are the average values of the atomic order parameter of carbon in the pure phases at the same conditions. The computed relative chemical potentials from the interface pinning calculations are shown in Fig. S23. To extend the chemical potentials to a wide range of pressures and temperatures, we used the thermodynamic integration method [22, 23], by numerically integrating the Gibbs–Duhem relation along isotherms and the Gibbs–Helmholtz relations along isobars, respectively.

#### D. Nucleation free energy of diamond from pure C liquid

To compute the nucleation free energy of diamond from undercooled liquid carbon, well-tempered metadynamics [24] simulations with adaptive bias [25] were performed using the PLUMED code [18] on pure carbon systems with 4,096 atoms in a cubic box. The simulation length was more than 200 ps. The relevant section in the PLUMED input file is reproduced below:

```
METAD ...
LABEL=metad
ARG=m3.morethan-1
PACE=400 HEIGHT=5.0 SIGMA=200 FILE=HILLS
TEMP=4000 BIASFACTOR=100
ADAPTIVE=DIFF SIGMA_MAX=200 SIGMA_MIN=0.1
... METAD

UPPER_WALLS ARG=m3.morethan-1 AT=800 KAPPA=0.2 LABEL=res
```

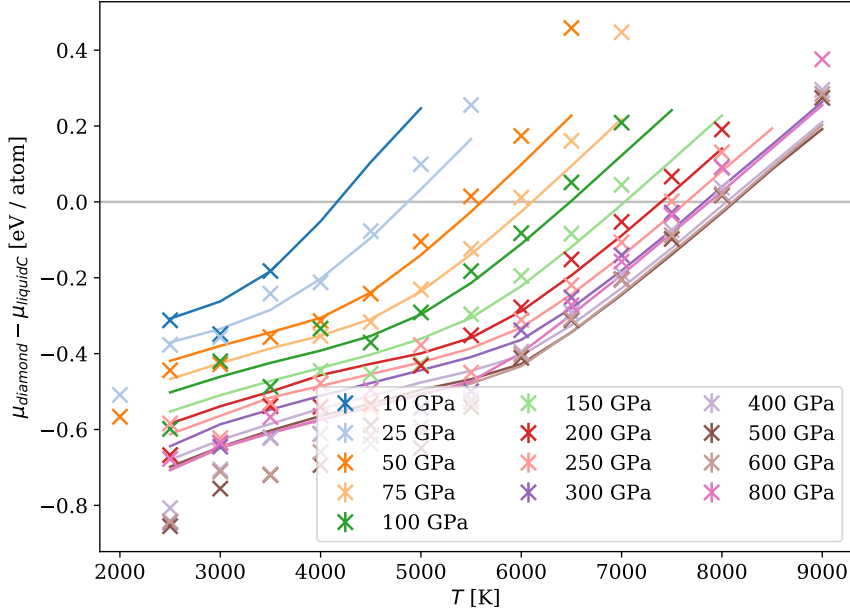


FIG. S23. The relative chemical potentials of diamond shown relative to the chemical potential of liquid carbon at each indicated pressure and temperature, computed at the MLP level in the interface pinning simulations. The error bars are smaller than the symbols. The solid lines in are not fits, but independently calculated from thermodynamic integration calculations using the MLP.

From the metadynamics simulations, we first calculated the free energy profiles as functions of the CV ( $m3.morethan-1$ ), and from these we extracted  $G(n_s)$  using the framework introduced in Ref. [26]. A Gibbs dividing surface with zero surface excess of the CV is implicitly assumed. The resulting free energy profiles (shown in Fig. S24), combined with the previously computed  $\Delta\mu_D$ , are then fitted to the CNT expression (Eqn.1 in the main text), to obtain the surface energy  $\gamma(36\pi)^{\frac{1}{3}}v_s^{\frac{2}{3}}$  at a wide range of conditions. From the CNT nucleation free energy profiles, we obtained the nucleation rate using [27, 28]

$$J = (1/v_l)Zf^+ \exp(-G^*/k_B T) \quad (6)$$

where  $v_l$  is the molar volume of the undercooled liquid,  $f^+$  is the addition rate of particles to the critical nucleus.

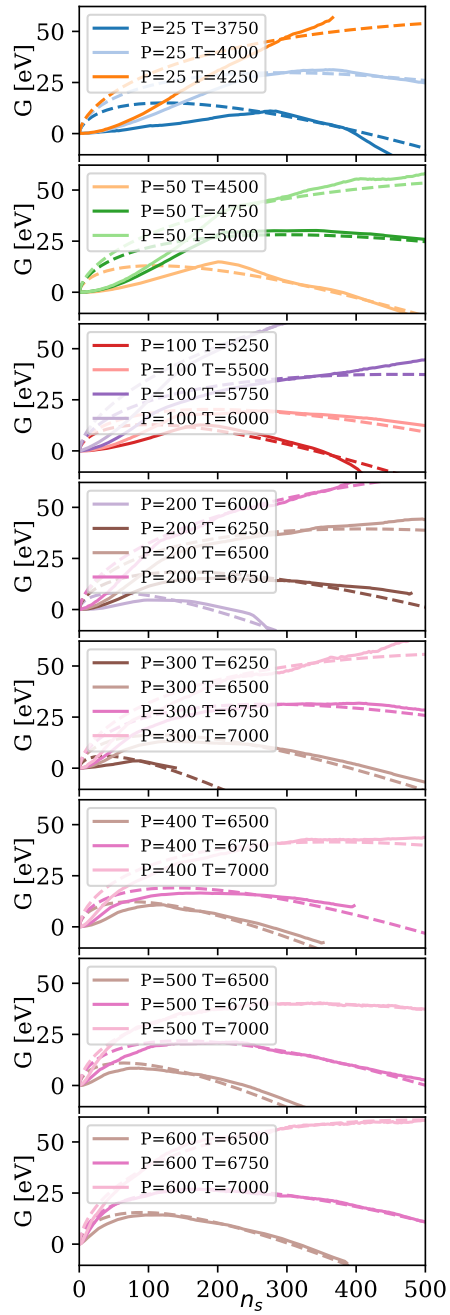


FIG. S24. Nucleation free energy profiles as functions of diamond nucleus sizes  $n_s$ , computed from metadynamics simulations using the MLP. The dashed curves are the fits to the CNT expression.



### E. Direct computation of the nucleation prefactor

We computed  $f^+$  accurately and directly at 50 GPa, 5000 K by applying a stochastic model. This model was originally proposed to mimic the kinetics of planar interfaces [29], and later extended to use in the case of homogeneous nucleation [30]. We used a combination of the umbrella sampling method and the seeding technique [31]: the fluid is first seeded with a pure diamond nucleus, and then an umbrella potential is added to the Hamiltonian of the system [32] to stabilize the nucleus (see Eqn. (4)). The system size was 4,096 carbon atoms, and the simulation length was 40 ps.

In the stochastic model, the time evolution of the collective variable  $\Phi$  is expressed as

$$\Phi(t) = (\phi_s - \phi_l)n_s(t) + \phi_l N + f(t). \quad (7)$$

The first term stems from the temporal change of the size  $n_s(t)$  of the solid cluster evolving under the biased Hamiltonian. The last term,  $f(t)$ , takes into account fluctuations that do not change the composition of the solid-liquid system, but are due to changes of the extensive quantity  $\Phi$  within the bulk phases. In general, the time evolution of these two terms in Eqn. (7) occurs on distinct time scales. These different time scales are reflected in the power spectrum  $S(\omega)$  of  $\Phi(t)$ , related to the time autocorrelation function  $\langle \Phi(0)\Phi(t) \rangle$  by

$$S(\omega) = \int_{-\infty}^{\infty} \langle \Phi(0)\Phi(t) \rangle e^{-i\omega t} dt. \quad (8)$$

In Fig. S25 we plot  $\omega S(\omega)$  obtained for a solid-liquid system that contains a diamond nucleus of about 500 atoms (green curve) at 50 GPa, 5000 K. For comparison, we also show the results for the reference bulk solid and bulk liquid (500 bulk solid atoms and 3,596 bulk liquid atoms) under the same thermodynamic conditions. Only for the solid-liquid system with a nucleus there is another well separated peak at a frequency of about  $10^3 \text{ ps}^{-1}$ , which stems from the growth of the crystal embedded in the liquid.

To rationalize the power spectrum  $S(\omega)$  further and extract quantitative information on the growth process from it, we postulate that the time evolution of the collective variable  $\Phi(t)$  can be modeled using a pair of coupled Langevin equations as described in Ref. 29:

$$\gamma \dot{q} = -\kappa(f + q - \bar{\Phi}) + \eta(t) \quad (9)$$

$$m_f \ddot{f} = -\kappa_f f - \kappa(f + q - \bar{\Phi}) - \gamma_f \dot{f} + \eta_f(t), \quad (10)$$

where the variable  $q$ , representing the slowly evolving part of  $\Phi$ , is defined as  $q = (\phi_s - \phi_l)n_s(t) + \phi_l N$ . In the above equation,  $\gamma$  and  $\gamma_f$  are friction constants associated with  $q$  and  $f$ , respectively,

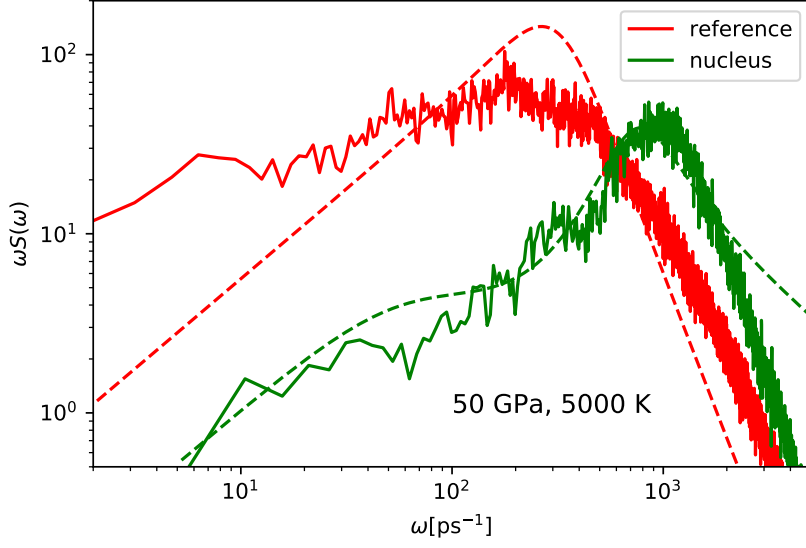


FIG. S25. The green curve is the spectrum  $\omega S(\omega)$  for the coexistence system with a solid nucleus ( $n_s = 500$ ) at 5000 K and 50 GPa. The red curve is the spectrum for a reference system made of pure bulk phases. The dashed green curve is the fitting curve using Eqn. (11) with parameters  $m_f = 5 \times 10^{-6}$  ps<sup>2</sup> kJ/mol,  $\kappa_f = 0.5$  kJ/mol,  $\gamma_f = 0.002$  ps kJ/mol, and  $\gamma = 0.005$  ps kJ/mol.

$\eta(t)$  and  $\eta_f(t)$  are Gaussian random forces. While the dynamics of  $q(t)$  are assumed to be overdamped, inertial effects are included for the variable  $f(t)$ , which is assigned an effective mass of  $m_f$ . The force constant  $\kappa$  is the sum of the umbrella spring constant of value 2 kJ/mol and the curvature of the free energy for the nucleus (which is negligible in this case). For this model, the power spectrum  $S(\omega)$  of  $\Phi(t)$  is

$$S(\omega) = \frac{2k_B T}{\omega^2} \text{Re} \left[ \left[ \frac{1}{\gamma} + \left[ \gamma_f + i \left( \omega m_f - \frac{\kappa_f}{\omega} \right) \right]^{-1} \right]^{-1} - \frac{i\kappa}{\omega} \right]^{-1}. \quad (11)$$

We fitted this expression to the power spectrum obtained from the umbrella sampling simulation and the result is shown in Fig. S25. As can be inferred from the figure, the simple Langevin model captures both peaks of the power spectrum. From the fit, we obtained  $\gamma = 0.005$  ps kJ/mol, yielding an addition rate of particles to the 500-atom nucleus of  $f^+ = 8 \times 10^{15}$  s<sup>-1</sup>.

## F. Estimate of $f^+$ at other conditions

A reasonable estimate for the addition rate  $f^+$  is [33]

$$f^+ \propto D n_s^{2/3}, \quad (12)$$

where  $n_s$  is the size of the nucleus and  $n_s^{2/3}$  is thus proportional to the surface area,  $D$  is the diffusion coefficient of the atoms. Here, we take the diffusion coefficient of liquid carbon shown in Fig. S22, and use the computed value of  $f^+$  for a 500-atom nucleus at  $T=5000$  K at  $P=50$  GPa ( $f^+(n = 500, P = 50, T = 5000) = 8 \times 10^{15} \text{ s}^{-1}$ ), and estimate  $f^+$  for critical nuclei at other conditions by

$$f^+(n_s^*, P, T) = f^+(500, 50, 5000) \frac{D(P, T)}{D(50, 5000)} (n_s^*/500)^{2/3}. \quad (13)$$

## G. Chemical potential of C in C/H mixtures

The S0 method for computing the chemical potentials in a mixture only uses equilibrium MD NPT simulations of C/H mixtures with carbon fraction  $\chi_C$ . In practice, we started with a pure carbon system of 64 C atoms, adding different amounts of hydrogen atoms (1, 2, 4, 6, 8, 12, 16, 24, 32, 40, 48, 56, 64, 72, 80, 88, 96, 104, 112, 128, 144, 160, 192, 224, 256, 288, 352, 384, 448, 512, 672, 768, 896, 1024, 1280, 1536, 2048, 2560, 3072), and then replicated the simulation box a few times in all dimensions such that the total number of atoms are roughly between 10,000 and 100,000. For each run, the simulation length was about 10 ps.

In Fig. S26 we show a snapshot from a MD run, where the liquid-liquid phase separation (PT2) can be observed.

Interface pinning simulations [29, 30] were performed on a diamond–C/H liquid coexistence system containing 1,024 C atoms and varying number of H atoms (ranging from 128 to 2,560) at pressures between 0 GPa and 600 GPa. The simulation time was about 50 ps. A snapshot of the coexistence system is in the Fig. S27. The simulations are performed using umbrella sampling based on the locally averaged Q3 order parameter as described before.

## H. Hydrocarbon crystals

The C/H system can form a large variety of crystal structures, which have been probed from DFT crystal structure searches [34–38]. The current understanding is that  $\text{CH}_4$  will decompose into

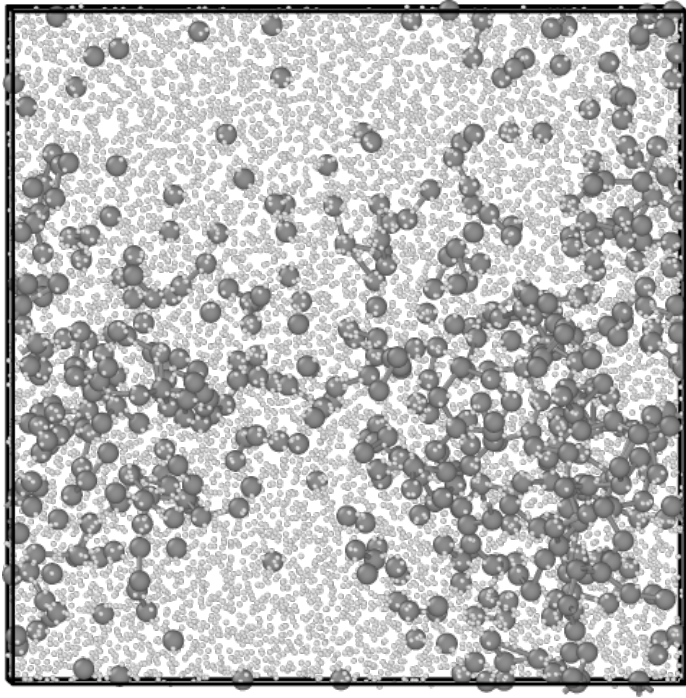


FIG. S26. A snapshot of the atomic coordinates from MD simulations at  $P=400$  GPa,  $T=3000$  K. The system contains 512 carbon atoms and 10,240 hydrogen atoms. Carbon atoms are shown as gray spheres, and hydrogen atoms are shown as white spheres.

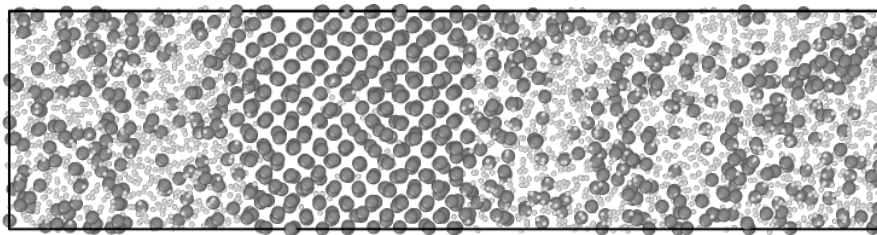


FIG. S27. An illustration of the simulation setup used in the coexistence simulations for computing the chemical potential difference between diamond and the carbon atoms dissolved in the C/H mixture. Carbon atoms are shown as gray spheres, and hydrogen atoms are shown as white spheres.

diamond and hydrogen at 0 K and pressures above 300 GPa (considering zero-point energies) [36, 37], CH<sub>2</sub> and CH can form diamond and lighter C/H crystals at 0 K and pressures above about 20 GPa (considering zero-point energies) [37]. For finite-temperature free energies, harmonic approximation suggests that lattice vibrations massively stabilize the diamond phase, making it the most stable composition at temperatures high than about 1000 K-3000 K [36]. Furthermore, the melting point of CH<sub>4</sub> crystals is between 1000 K and 1500 K. Indeed, in our DFT MD and MLP MD simulations, CH<sub>4</sub> crystals melt quickly at  $T \geq 2000$  K. This means that the C/H crystals are less stable than either liquid or diamond at the temperature range considered for diamond formation in this work ( $T \geq 3000$  K). As such, the possible formation of C/H crystals are not relevant in the current study.

## VI. CARBON CONTENTS OF PLANETS AND STARS

We highlight here a few examples of carbon and hydrogen mixtures found in giant planets and carbon-rich stars.

### A. Atmosphere

The measured elemental abundance in the atmosphere of Neptune and Uranus is taken from Table 3 in Ref. [39]. To go from the ratios to concentrations we assume that these elements are the totality of elements present, i.e.  $[C] + [He] + [S] + [H] = 1$ , divide each side by the concentration of hydrogen to get  $[C]/[H] + [He]/[H] + [S]/[H] + 1 = 1/[H]$  which, given the measured abundance ratios, can be solved to get the concentration of hydrogen and other elements. For Uranus the elemental ratios are:  $He/H = 0.09 \pm 0.02$ ,  $C/H = 0.0236 \pm 0.003$  and  $S/H = 0.00032 \pm 0.00016$ . Hence,

$$[C] + [He] + [S] + [H] = 1$$

$$0.0236 + 0.09 + 0.00032 + 1 = 1/[H]$$

$$[H] = 0.8977$$

$$[C]/[H] = 0.0236; [C] = 0.0212$$

$$[He]/[H] = 0.09; [He] = 0.0808$$

$$[S]/[H] = 0.00032; [S] = 0.0003$$

Measured elemental abundance ratios in Neptune are similar to Uranus:  $He/H = 0.117 \pm 0.02$ ,

$C/H = 0.0247 \pm 0.0062$  and  $S/H = 0.00032 \pm 0.00016$ . Concentrations are:

$$[C] + [He] + [S] + [H] = 1$$

$$0.0247 + 0.117 + 0.00032 + 1 = 1/[H]$$

$$[H] = 0.8756$$

$$[C]/[H] = 0.0247; [C] = 0.0216$$

$$[He]/[H] = 0.117; [He] = 0.1025$$

$$[S]/[H] = 0.00032; [S] = 0.0003$$

The concentration of carbon in both planets is about 2%.

### B. Neptune and Uranus interior models

Elemental abundances in the interior of the ice giant planets are model dependent, since they are generally not accessible to direct measurements. Recent Uranus models by Nettelmann *et al.* [40] use equations of state for  $CH_4$ ,  $NH_3$  and  $H_2O$  that are linearly mixed in the inner envelope with  $(CH_4:NH_3:H_2O)$  proportions of (4:1:7.7). In terms of elemental ratios this is equivalent to  $C/H = 0.1162$ ,  $N/H = 0.0291$  and  $O/H = 0.2238$ . Concentration are:

$$[C] + [N] + [O] + [H] = 1$$

$$0.1162 + 0.0291 + 0.2238 + 1 = 1/[H]$$

$$[H] = 0.7304$$

$$[C]/[H] = 0.1162; [C] = 0.0849$$

$$[N]/[H] = 0.0291; [N] = 0.0213$$

$$[O]/[H] = 0.2238; [O] = 0.1635$$

The concentration of carbon is about 8% in these interior models with a pressure range between 10 GPa and 550 GPa for the inner envelope.

### C. White Dwarfs

Recently, Hollands *et al.* reported an example of a White Dwarf star with a mixed carbon-hydrogen atmosphere with a  $C/H$  ratio of 0.15 [41]. Helium was not detected in the spectra hence the carbon and hydrogen concentrations are 13% and 87% respectively. Deeper in the star the composition is thought to be a mixture of carbon, oxygen and neon.

- 
- [1] G. Kresse and J. Hafner, “Ab initio molecular dynamics for liquid metals,” *Phys. Rev. B* **47**, 558 (1993).
- [2] G. Kresse and J. Hafner, “Ab initio molecular-dynamics simulation of the liquid-metal-amorphous-semiconductor transition in germanium,” *Phys. Rev. B* **49**, 14251 (1994).
- [3] G. Kresse and J. Furthmüller, “Efficient iterative schemes for ab initio total-energy calculations using a plane-wave basis set,” *Phys. Rev. B* **54**, 11169 (1996).
- [4] J. P. Perdew, K. Burke, and M. Ernzerhof, “Generalized gradient approximation made simple,” *Phys. Rev. Lett.* **77**, 3865 (1996).
- [5] M. French, T. R. Mattsson, N. Nettelmann, and R. Redmer, “Equation of state and phase diagram of water at ultrahigh pressures as in planetary interiors,” *Phys. Rev. B* **79**, 054107 (2009).
- [6] S. Nosé, “A unified formulation of the constant temperature molecular-dynamics methods,” *J. Chem. Phys.* **81**, 511 (1984).
- [7] M. Bethkenhagen, E. R. Meyer, S. Hamel, N. Nettelmann, M. French, L. Scheibe, C. Ticknor, L. A. Collins, J. D. Kress, J. J. Fortney, and R. Redmer, “Planetary ices and the linear mixing approximation,” *Astrophys. J.* **848**, 67 (2017).
- [8] J. Behler and M. Parrinello, “Generalized neural-network representation of high-dimensional potential-energy surfaces,” *Phys. Rev. Lett.* **98**, 146401 (2007).
- [9] A. Singraber, T. Morawietz, J. Behler, and C. Dellago, “Parallel multistream training of high-dimensional neural network potentials,” *Journal of Chemical Theory and Computation* **15**, 3075 (2019).
- [10] P. Rowe, V. L. Deringer, P. Gasparotto, G. Csányi, and A. Michaelides, “An accurate and transferable machine learning potential for carbon,” *J. Chem. Phys.* **153**, 034702 (2020).
- [11] V. L. Deringer and G. Csányi, “Machine learning based interatomic potential for amorphous carbon,” *Physical Review B* **95** (2017), 10.1103/physrevb.95.094203.
- [12] B. Cheng, R.-R. Griffiths, S. Wengert, C. Kunkel, T. Stenczel, B. Zhu, V. L. Deringer, N. Bernstein, J. T. Margraf, K. Reuter, *et al.*, “Mapping materials and molecules,” *Accounts of Chemical Research* **53**, 1981 (2020).
- [13] B. Cheng, G. Mazzola, C. J. Pickard, and M. Ceriotti, “Evidence for supercritical behaviour of high-pressure liquid hydrogen,” *Nature* **585**, 217 (2020).

- [14] C. J. Pickard and R. J. Needs, “Ab initio random structure searching,” *Journal of Physics: Condensed Matter* **23**, 053201 (2011).
- [15] S. Plimpton, “Fast Parallel Algorithms for Short-Range Molecular Dynamics,” *J. Comput. Phys.* **117**, 1 (1995).
- [16] A. Singraber, J. Behler, and C. Dellago, “Library-based LAMMPS implementation of high-dimensional neural network potentials,” *J. Chem. Theory Comput.* **15**, 1827 (2019).
- [17] U. R. Pedersen, F. Hummel, G. Kresse, G. Kahl, and C. Dellago, “Computing gibbs free energy differences by interface pinning,” *Phys. Rev. B* **88**, 94101 (2013).
- [18] G. A. Tribello, M. Bonomi, D. Branduardi, C. Camilloni, and G. Bussi, “Plumed 2: New feathers for an old bird,” *Comput. Phys. Commun* **185**, 604 (2014).
- [19] W. Lechner and C. Dellago, “Accurate determination of crystal structures based on averaged local bond order parameters,” *J. Chem. Phys.* **129**, 114707 (2008).
- [20] P. J. Steinhardt, D. R. Nelson, and M. Ronchetti, “Bond-orientational order in liquids and glasses,” *Physical Review B* **28**, 784 (1983).
- [21] B. Cheng, G. A. Tribello, and M. Ceriotti, “Solid-liquid interfacial free energy out of equilibrium,” *Phys. Rev. B* **92**, 180102 (2015).
- [22] B. Cheng and M. Ceriotti, “Computing the absolute Gibbs free energy in atomistic simulations: Applications to defects in solids,” *Phys. Rev. B* **97**, 054102 (2018).
- [23] A. Reinhardt and B. Cheng, “Quantum-mechanical exploration of the phase diagram of water,” *Nat. Commun.* **12**, 1 (2021).
- [24] A. Barducci, G. Bussi, and M. Parrinello, “Well-tempered metadynamics: a smoothly converging and tunable free-energy method,” *Phys. Rev. Lett.* **100**, 20603 (2008).
- [25] D. Branduardi, G. Bussi, and M. Parrinello, “Metadynamics with adaptive gaussians,” *J. Chem. Theory Comput.* **8**, 2247 (2012).
- [26] B. Cheng and M. Ceriotti, “Bridging the gap between atomistic and macroscopic models of homogeneous nucleation,” *J. Chem. Phys.* **146**, 34106 (2017).
- [27] S. Auer and D. Frenkel, “Prediction of absolute crystal-nucleation rate in hard-sphere colloids,” *Nature* **409**, 1020 (2001).
- [28] J. Espinosa, C. Navarro, E. Sanz, C. Valeriani, and C. Vega, “On the time required to freeze water,” *J. Chem. Phys.* **145**, 211922 (2016).



- [29] U. R. Pedersen, F. Hummel, and C. Dellago, “Computing the crystal growth rate by the interface pinning method,” *J. Chem. Phys.* **142**, 44104 (2015).
- [30] B. Cheng, C. Dellago, and M. Ceriotti, “Theoretical prediction of the homogeneous ice nucleation rate: Disentangling thermodynamics and kinetics,” *Phys. Chem. Chem. Phys.* **20**, 28732 (2018).
- [31] J. R. Espinosa, C. Vega, C. Valeriani, and E. Sanz, “Seeding approach to crystal nucleation,” *J. Chem. Phys.* **144**, 34501 (2016).
- [32] G. M. Torrie and J. P. Valleau, “Nonphysical sampling distributions in monte carlo free-energy estimation: Umbrella sampling,” *Journal of Computational Physics* **23**, 187 (1977).
- [33] K. F. Kelton, “Crystal nucleation in liquids and glasses,” in *Solid state physics*, Vol. 45 (Elsevier, 1991) pp. 75–177.
- [34] G. Gao, A. R. Oganov, Y. Ma, H. Wang, P. Li, Y. Li, T. Iitaka, and G. Zou, “Dissociation of methane under high pressure,” *J. Chem. Phys.* **133**, 144508 (2010).
- [35] H. Liu, I. I. Naumov, and R. J. Hemley, “Dense hydrocarbon structures at megabar pressures,” *J. Phys. Chem. Lett.* **7**, 4218 (2016).
- [36] A. S. Naumova, S. V. Lepeshkin, and A. R. Oganov, “Hydrocarbons under pressure: Phase diagrams and surprising new compounds in the c-h system,” *J. Phys. Chem. C* **123**, 20497 (2019).
- [37] L. J. Conway and A. Hermann, “High pressure hydrocarbons revisited: from van der Waals compounds to diamond,” *Geosciences* **9**, 227 (2019).
- [38] T. Ishikawa and T. Miyake, “Evolutionary construction of a formation-energy convex hull: Practical scheme and application to a carbon-hydrogen binary system,” *Phys. Rev. B* **101**, 214106 (2020).
- [39] T. Guillot and D. Gautier, “10.16 - giant planets,” in *Treatise on Geophysics (Second Edition)*, edited by G. Schubert (2015) second edition ed., pp. 529–557.
- [40] N. Nettelmann, K. Wang, J. J. Fortney, S. Hamel, S. Yellamilli, M. Bethkenhagen, and R. Redmer, “Uranus evolution models with simple thermal boundary layers,” *Icarus* **275**, 107 (2016).
- [41] M. A. Hollands, P. E. Tremblay, B. T. Gänsicke, M. E. Camisassa, D. Koester, A. Aungwerojwit, P. Chote, A. H. Córscico, V. S. Dhillon, N. P. Gentile-Fusillo, M. J. Hoskin, P. Izquierdo, T. R. Marsh, and D. Steeghs, “An ultra-massive white dwarf with a mixed hydrogen–carbon atmosphere as a likely merger remnant,” *Nature Astronomy* **4**, 663 (2020).